Effect of Surface Condition on Resistance Spot Welding of Advanced High Strength Steel

by

Xu Han

A thesis
presented to the University of Waterloo
in fulfillment of the
thesis requirement for the degree of
Master of Applied Science
in
Mechanical and Mechatronics Engineering

Waterloo, Ontario, Canada, 2019

AUTHOR'S DECLARATION

This thesis consists of material all of which I authored or co-authored: see Statement of Contributions included in the thesis. This is a true copy of the thesis, including any required final revisions, as accepted by my examiners.
I understand that my thesis may be made electronically available to the public.

Statement of Contributions

This thesis was solely written by the candidate. Professors N. Zhou and E. Biro contributed to editing the entire thesis. Additional contributions were made by other members of the Centre for Advanced Material Joining group from University of Waterloo and Centre for Automotive Materials and Corrosion from McMaster University. The specific contributions are listed below.

Chapter 4 of this thesis is based on the results from a conference paper: X. Han, C. DiGiovanni, J. McDermid, E. Biro, N.Y. Zhou, "Effect of Internal Oxidation on the Weldability of CMnSi Steels." IIW Commission III intermediate meeting, 2019. The experimental design, analysis, and writing were conducted by the candidate. Some of the material's preparation procedures (material cleaning and selective oxidation of the CMnSi steel) were completed by personnel at the CAMC using the McMaster Galvanizer Simulator owned by Prof. J. Mcdermid. The paper was also co-authored by Prof. E. Biro, Prof. N.Y. Zhou, and Mr. C. Digiovanni who contributed through technical discussions of the results and assisted with editing the manuscript.

Chapter 5 of this thesis is based on the results from a conference paper: X. Han, M.H. Razmpoosh, A. Macwan, E. Biro, Y. Zhou, "Effect of Galvannealed Coating Condition on Weldability of 22MnB5 Press-hardened Steel." Sheet Metal Welding Conference XVII, 2018. The experimental design, analysis, and writing were conducted by the candidate. The paper was also co-authored by Prof. E. Biro, Prof. N.Y. Zhou, Mr. M.H. Razmpoosh, and Dr. A. Macwan from ArcelorMittal Dofasco, who contributed through technical discussions of the results and assisted with editing the manuscript.

Chapter 6 of this thesis used data obtained from chapters 4 and 5. Additional experimental work was completed using the material previously used in chapter 4 and 5.

Abstract

Advanced high strength automotive sheet steel (AHSS) is used in body-in-white design to reduce vehicle weight while maintaining high crashworthiness. Surface coatings applied to AHSS to protect it from oxidation and decarburization during its processing and life cycle. Due to the characteristics of AHSS, including alloying content and thermal process requirements, a variation of final surface conditions is possible. The resistance welding process is affected by surface changes as it alters the electrical contact resistance. As a result, a change in resistance spot welding process window occurs. Without proper attention, this variation in the operation window could reduce the joint strength and results in an unpredictable failure by having an undersized nugget. In this study, two surface-related phenomena, internal oxidation, and zinc diffusion, were investigated to characterize their impact on resistance spot welding. Additionally, a heat input based electrical dynamic resistance approach was proposed to determine appropriate welding current given variations in the Zn diffusion layer resulting from heat treating during this hot stamping process for PHS steels.

Promotion of internal oxidation is used in Zn galvanizing line to improve the wettability of the steel surface to the Zn pool via the enhancement of the reactive wetting. The presence of these internal oxides has shown to shift the weld lobe to higher currents, increasing the time required to generate an acceptable weld. Study of weld development showed that surface melting is responsible for this shift in the weld process window. The surface melting created a liquid contact surface between the faying surface, which reduced the electric contact resistance and heat generation at the weld faying surface. A smaller nugget was formed due to the reduction of heating. To compensate for this reduced heat generation, a higher welding current was required when RSW of internally oxidized samples.

Zinc diffusion from the galvannealed coating to the steel substrate occurs when a galvannealed steel was exposed to elevated temperature during heat treatment in the press-hardening process. This formed a Fe-Zn diffusion layer. The thickness and composition of the diffusion layer were found to be dependent on heat-treatment conditions. With an increase in heat-treatment time, the electrical resistance of the steel sheet was observed to increase as well. With higher electrical resistance, less welding current was needed to weld the material. While a change in nugget size occurred when welding steels made using different heat-treatment conditions with constant welding parameters, the mechanical lap shear strength was not impacted. Martensite tempering in the heat-affected region was more severe in samples with a larger diameter weld nugget, which decreased the required stress for failure to occur, counter-acting the increase in strength gained from the larger nugget size. This work has shown that with a heat-treatment time ranging between 4 to 10 minutes, a robust resistance welding schedule can be determined to generate a mechanically sound weld.

Dynamic electrical resistance has been used to monitor the weld quality. Heat input analysis was shown to reflect the weld development as it takes into account the full weld cycle. Heat input has shown to have a linear correlation with nugget size. Undersized nugget can be successfully detected and corrected by changing the welding current based on the heat input value calculated from dynamic resistance measurement.

Acknowledgments

I like to give my special thanks to my supervisors Prof. Norman Zhou and Prof. Elliot Biro for their time, guidance, and support throughout my master's study. Their guidance helps me not only academically, but also helps me to see the world from a new perspective.

I also wish to thank sponsors and collaborators including Dr. Andrew Macwan from ArcelorMittal Dofasco Hamilton, Dr. Joseph McDermid from McMaster University, and Dr. Frank Goodwin from the International Zinc Association for their support, knowledge, and generosity in providing the necessary material to complete this thesis. I am grateful to Prof. Mike Worswike of the MME department for granting access to the hot-stamping press. I would also like to thank Dr. Yuquan Ding and Mr. Mark Griffett for their advice on samples preparation methods and characterizing equipment.

In addition, I wish to acknowledge the assistance of my fellow CAMJ members, especially Chris DiGiovanni, Hadi Razmpoosh, Erica Wintjes, Josh He, Shehryar Khan, and Alireza Mohamadizadeh. The time we spend inside and outside the lab has made this experience memorable.

Finally, I wish to thank my family for their support, without which I would not be able to complete this degree.

Table of Contents

List of Figures

List of Tables

List of Symbols

α – Ferritic phase
Γ – Austenitic phase
A_{C1} – Austenite transformation start temperature
A_{C3} – Austenite transformation end temperature
c – A constant to determine the required minimum nugget size
I – Welding current
Q – Instantaneous heat generation
Q_{Total} – total heat generation through the welding cycle
R – Electrical resistance
t – welding time
t_s – Steel sheet thickness

List of abbreviations

A - Austenite
AHSS – Advanced high strength steel
B – Bainite
BCC – Body-centered cubic
BCT – Body-centered tetragonal
BIW – Body-in-white
BM – Base material
CGL – Continuous galvanizing line
CP – Complex phase
DP – Dual-phase
EDX – Energy-dispersive X-ray
EPMA – Electron probe microanalysis
F - Ferrite
FCC – Face-centered cubic
FZ – Fusion zone
GA – Galvannealed Zn coating
GI – Galvanized Zn coating
HAZ – Heat affected zone
M – Martensite
MFDC – Medium frequency direct current
MGS – McMaster galvanizing simulator
MS – Martensitic steel
PHS – Press-hardening steel
QP – Quench and partitioned
RA – Retained austenite
RSW – Resistance spot welding
SEM – Scanning electron microscopy
TRIP – Transformation induced plasticity
TWIP – Twinning induced plasticity
UHSS – Ultimate high strength steel
UTS – Ultimate tensile strength

Chapter 1 Introduction

1.1 Overview

Application of coating on advanced high strength steel is a common practice to protect the steel surface from oxidation and decarburization in its production and service life. Different coating and manufacturing processes can lead to a varied final surface condition in advanced high strength steel. The resistance welding process is affected by surface changes as it alters the electrical contact resistance. As a result, a change in resistance spot welding process window occurs. Without proper attention, this variation in the operation window could reduce the joint strength and results in an unpredictable failure by having an undersized nugget.

1.2 Problem and Justification

With the increasing concern in global warming, governmental agencies have issued stringent regulations on the automotive industry to reduce its emission and carbon footprint. Corporate Average Fuel Economy (CAFÉ) has been set-up in North America by the US Environmental Protection Agency and National Highway Traffic Safety Administration, and similar regulations are in place for Europe and the rest of the world. The emission target of 95 grams of CO2 per kilometer per fleet average was set for 2021, which roughly converts to a fuel consumption of 4.1 L per 100 km [1]. A harsh penalty is exerted on the manufacturers to motivate the reduction in fuel consumption. The vehicle weight reduction is proposed to achieve these targets. With reduced body weight, vehicles can achieve a higher mileage in gasoline vehicles and an extended range in electric vehicles [2]. Non-ferrous materials such as the aluminum or fiber-reinforced alloys can provide a minimum weight while achieving a higher strength. However, their high material and manufacturing costs are not suitable for mass production in the public market [3], [4]. Advanced high strength steel became the optimum choice for weight reduction in vehicle body with enhanced strength and ductility, both

of which are greater than the conventional mild steel. The increased strength and ductility in AHSS satisfy the safety requirement while reducing the weight of the vehicle body [5]. While the mechanical properties of the advanced high strength steels are excellent, these steels require additional processing steps in their production cycle such as selective oxidation and press-hardening [6]–[8]. Due to the high alloying content and specially designed microstructure of the advanced high strength steel, it is more vulnerable to the processing environment. Surface coatings are required to protect the advanced high strength steel from corrosion and decarburization which are detrimental to the steel's mechanical properties [9], [10]. Changes in surface coating condition have been shown to affect the resistance spot welding (RSW) [11], a commonly used joining technic in the automotive industry. Current literature has looked at the effect of different coating types, but overlooked the process that could change the surface condition [11], [12]. It is important to understand the impact of a varied surface layer on the resistance spot welding behavior to avoid unexpected failures of the welded joint.

1.3 Objectives

The objective of this thesis is to analyze the effect of surface condition variations on the resistance spot welding behavior of the advanced high strength steel and their impact on the final mechanical properties of the RSW joint. Specific objectives include:

1) Evaluate the effect of selective internal oxidation on the welding behavior of CMnSi steels.

2) Characterize the diffusion layer created by heat treatment layer and its influence on the RSW process.

3) Use of dynamic electric resistance measurement to monitor and control the RSW process.

1.4 Thesis outline

The chapters in this thesis will be formatted as following:

1) Introduction – An introduction to the motivation, objective, and format of this thesis.

2) Literature Review – A summary of current literature on the field of AHSS, surface coating, RSW, and effect of surface condition on RSW process. It also shows how this work fits into the literature and the gaps it intends to fill.

3) Methodology – It shows the materials, welding equipment, and characterization methods used in this work.

4) Effects of Internal Oxides on Resistance Spot Welding– A study showing how the internal oxide affects the processing window, heat generation, and nugget development in RSW.

5) Effect of variation in Zn diffusion layer in Press-hardening Steel on its RSW Process - A study showing the effect of different Zn diffusion layer, a result of changes in heat-treatment condition, on the RSW process of PHS.

6) Heat Input Analysis of Dynamic Resistance for Monitoring and Controlling RSW Process – A study of the feasibility of using dynamic resistance value to monitor and control the RSW process to eliminate defects formation due to variations in surface condition.

7) Conclusion and recommendation – A summary of the work included in this thesis and suggested directions for future study.

Chapter 2 Literature Review

2.1 Advanced High Strength Steel (AHSS)

2.1.1 Modern Steels in the Automotive Industry

Steels have been widely used in the automotive industry as they are easy to process, provide high strength, and have a low cost. With the increase in environmental concerns, more stringent fuel economy standards have been implemented [1]. Lightweighting of the vehicle body-in-white (BIW) structure has been shown to be effective at reducing fuel consumption and improve fuel efficiency. While reducing the vehicle weight, the BIW must maintain its crashworthiness to maintain passenger protection. Advanced high strength steel (AHSS) have been developed to satisfy the requirement of lightweighting while maintaining crashworthiness. AHSS succeeded at improving the strength to ductility ratio by increasing both the strength and ductility compared to the conventional steels (Fig. 2.1a). To further improve the anti-intrusion capability of the passenger compartment, AHSS with even higher tensile strength (UTS > 980 MPa), often referred as ultimate high strength steel (UHSS), was used to prevent deformations in a crash scenario due to its exceptional tensile strength.

2.1.2 Different Grades of AHSS

The first generation AHSS and UHSS were the dual-phase steel (DP), transformation induced plasticity steel (TRIP), martensitic (MS), and press-hardening steel (PHS). DP and TRIP steels are mainly used as an energy-absorbing component due to their high strength, ductility, and work-hardening properties (Fig. 2.1b) [13]. On the other hand, MS and PHS are used in anti-intrusion components as their high yield strength resists deformation under a crash scenario to protect the passengers (Fig. 2.1b). The second-generation AHSS, twin-induced plasticity steel (TWIP), has an even better performance compared to the previous AHSS with further increase ductility; however, the expensive cost associated with TWIP steel production limited its application in the automotive industries [5]. Therefore, researchers have focused on the development of the affordable 3rd generation AHSS, such as complex phase steel (CP) or quench &partitioned steel (Q&P), which further improved mechanical properties compared to the first generation of AHSS [5]. For the purpose of this thesis, TRIP and PHS are studied due to their special processing and production steps of selective internal oxidation for the TRIP (further discussion in section 2.2.6) and the press-hardening for the PHS (section 2.1.5).

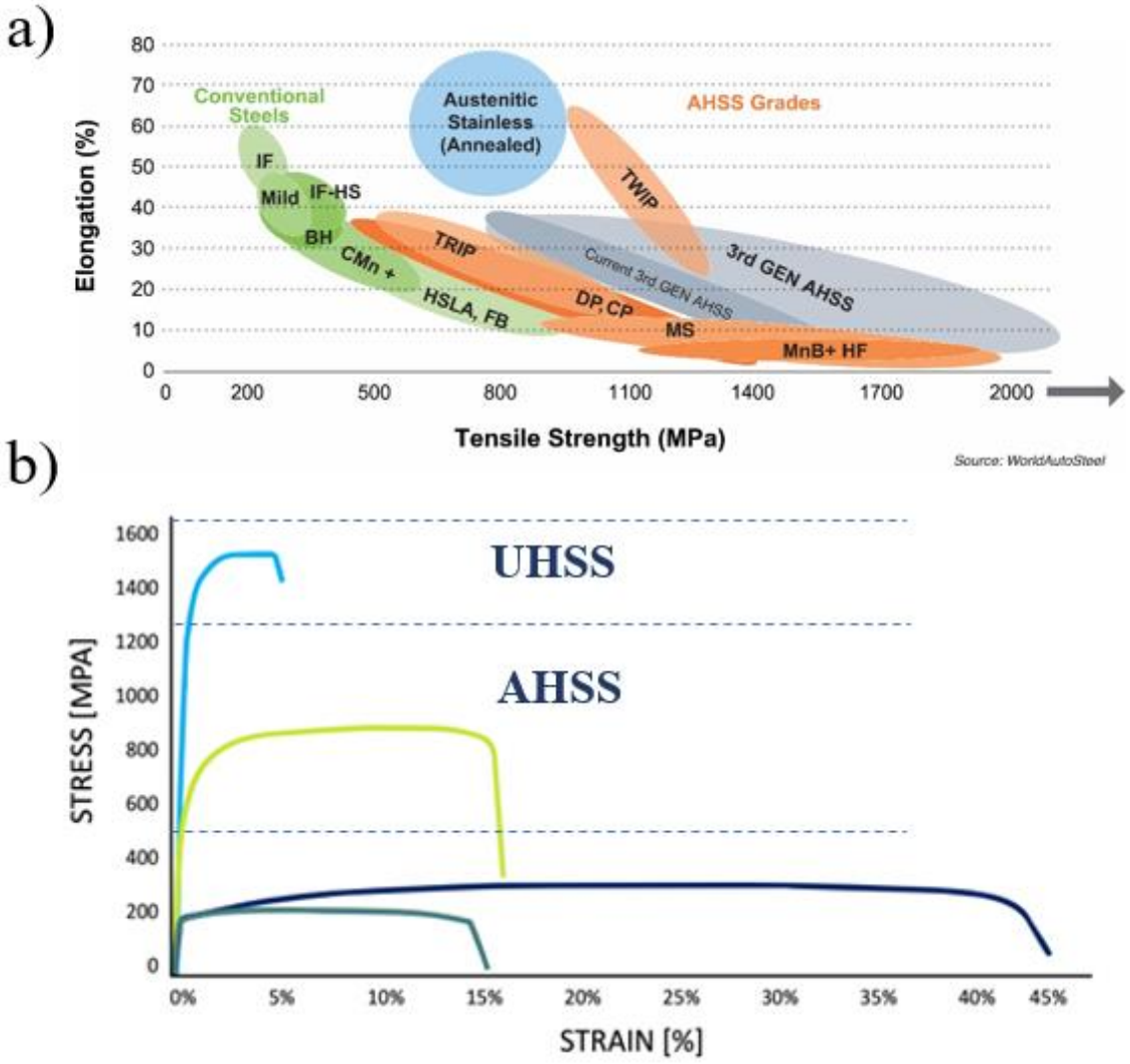

Figure 2.1 a) Chart summarizing the tensile strength and elongation region for various metals and b) the typical stress-strain curves for UHSS, AHSS, and mild steel. [14]

2.1.3 Transformation Induced Plasticity (TRIP) Steel

TRIP steel has a microstructure that is made of a ferrite (F) matrix with dispersed martensite (M), bainite (B), and retained austenite (RA) islands. The harder phase (M/B/RA) gives the strength to the material, and the softer phase matrix (F) provide the ductility. Compare to other AHSS such as DP steel, TRIP steel's RA phase within the ferrite matrix transforms into M when strained, further improving the work-hardening ability of the TRIP steel, which increases its ductility [15]. Alloying elements such as carbon, manganese, and silicon are mainly added to the TRIP steel to obtain this

desired structure and improve its performance. The carbon content helps to stabilize the austenite phase, Mn improves the solid solution strengthening in ferrite, and Si improves the hardenability [16]–[18].

2.1.4 Press-hardening Steel (PHS)

PHS is extensively used in the automotive industry due to its exceptional strength and formability allowing PHS to be used for anti-intrusive components in the passenger vehicle [19], [20]. The hot-stamping process offers PHS good formability, as it is formed hot, which allows the mass production of complex PHS parts while maintaining its high strength from the fully martensitic structure (Fig. 2.2). PHS material usually contains the boron as an alloying element. The addition of boron lowers the critical cooling rates to obtain the fully martensitic structure (Fig. 2.3), as boron may have segregated to the α/γ phase interface to inhibit ferrite regrowth during the quenching process [21], [22].

2.1.5 The Hot-stamping Process

PHS can be hardened and formed simultaneously using the hot-stamping process (Fig. 2.2). In the hot stamping process, the PHS is first decoiled and blanked into the desired shape. The blank is then transferred into a furnace and heated above its austenitization temperature (Ac_3) and held to achieve a fully austenitic structure. The heated blank is then transferred to the stamping press using a robot to ensure a quick transfer without temperature loss. A cooled die is then used to form and quench the blank to obtain a fully martensitic transformation at a high cooling rate. This hot-stamping process allows productions of complex parts to be made having a fully martensitic structure.

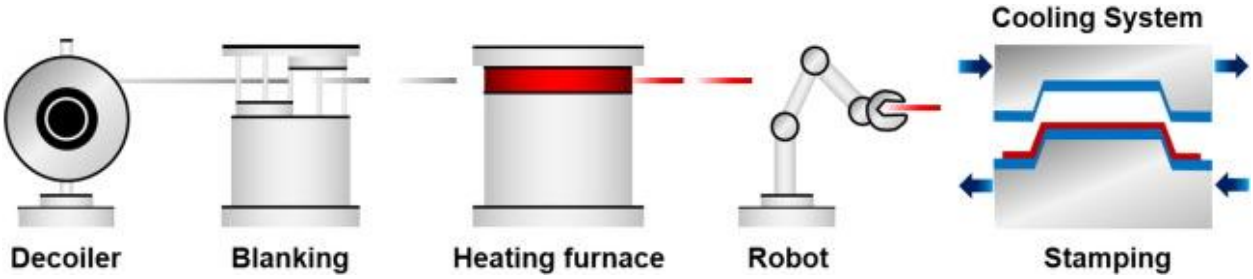

Figure 2.2 Hot-stamping process of the press-hardening steel featuring: 1) Steel feeds in from coils, 2) blanking into desired shape, 3) heat-treatment in furnace to achieve fully austenitic microstructure, 4) transfer into the stamping press via robot arm, and 5) press-

hardening using a cooled die where the material is formed and hardened via the high cooling. [23]

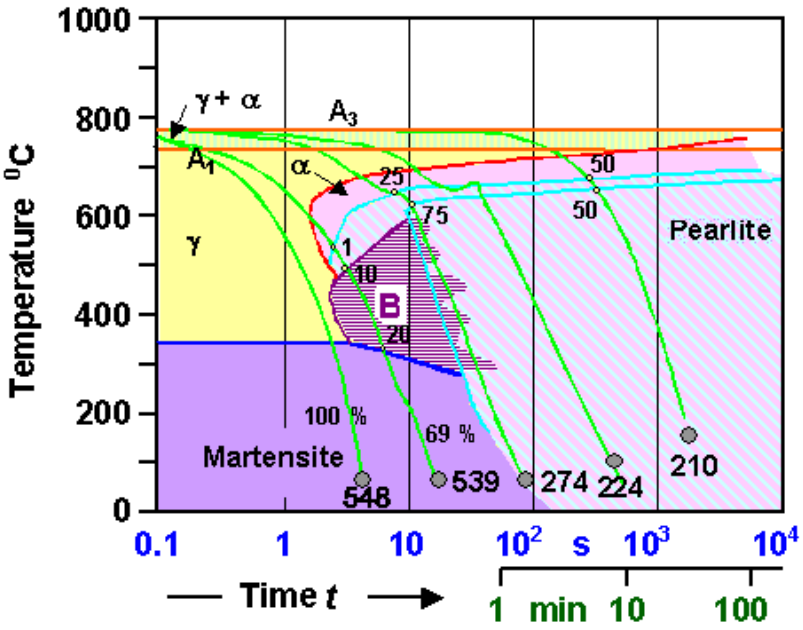

Figure 2.3 Continuous cooling transformation (CCT) diagram of carbon steel showing how the addition of boron allows martensitic transformations to occur at a lower cooling rate [24]**.**

2.1.6 Microstructures in AHSS

It is important to understand the different steel phases to study the behavior of AHSS, as AHSS has acquired its exceptional mechanical performance through its engineered phase ratio and microstructures [13], [25]. Some of the typical steel phases will be discussed in this section.

Austenite

Austenite has a face-centered cubic (FCC) crystal structure which allows higher solubility of carbon inside the grains [25]. Transformation to the austenitic structure occurs above the austenitization temperature (AC). The austenitization temperature can be found on the steel binary phase diagram with an example shown in Fig. 2.4. A_{C1} temperature indicates the start of the austenitization process and A_{C3} temperature indicates a full transformation is completed. The A_{C3} temperature ranges from 700 to 900 °C depending on steel chemical composition, where C has the most influence (Fig 2.4). Upon cooling, the unstable austenite transforms into the other phases such

as ferrite, pearlite, bainite, or martensite depending on the cooling rate and alloying state of the material (Fig. 2.3).

Retained Austenite

With the addition of alloying elements such as C, Mn, and Si, metastable austenite phases can be formed at room temperature, called retained austenite (RA). When the RA with low stability (which depends on the chemical composition, particle size, and distribution of the RA) is under an applied tension, it transforms into martensite due to the shear strain and dislocations. This transformation process offers a great ductility through the shear strain strengthening, and good strength due to the final martensite, and this strengthening process is named transformation induced plasticity (TRIP) effect due to the martensite transformation.

Ferrite

Compared to austenite, the ferritic microstructure is a stable steel phase at room temperature with its body-centered cubic (BCC) structure [25]. The ferrite structure is soft and ductile due to the BCC structure's low carbon solubility and low carbon content compared to the FCC microstructures. With the low carbon solubility of ferrite, the carbon content diffuses out of the grain, forming a carbon-rich phase called cementite on the grain boundary or within the grain. The ferritic structure can be obtained by slowly cooling the steel from its austenitic structure as shown in the CCT diagram (Fig. 2.3). Ferrite is mostly present in dual-phase steel to provide ductility to the material. Alloying elements like Zn and Al serves as ferrite stabilizer which promotes the formation of ferrite.

Martensite

The martensitic structure is a metastable phase with extremely high hardness. Martensite has a body-centered cubic (BCC) or body-centered tetragonal (BCT) crystal structure depending on the carbon content of the steel [25]. Martensite's crystal structure has a high density of dislocation due to the high carbon content. The high strength of martensite come from carbon atoms being trapped in the steel matrix, forming many dislocations which prevent the slip planes formation [26]. Lack of slip planes causes martensite to be strong but brittle at the same time. To obtain the metastable martensite phase, it usually is necessary for the steel to be cooled from the austenite phase field at a rate which is sufficiently fast to avoid all other solid-state transformations such as ferrite and pearlite [27] (Fig. 2.3). This cooling rate can be very high for plain carbon steels but quite slow for a heavily alloyed steel containing large concentrations of austenite stabilizing solute. During the rapid cooling, the transformation of austenite to martensite is a diffusionless process, where the shearing of the lattice forms the final BCC (low carbon content) or BCT (high carbon content) structure [28]. This

transformation is often accompanied by volume expansion due to the lower density of the BCC/BCT structure compared to the FCC structure.

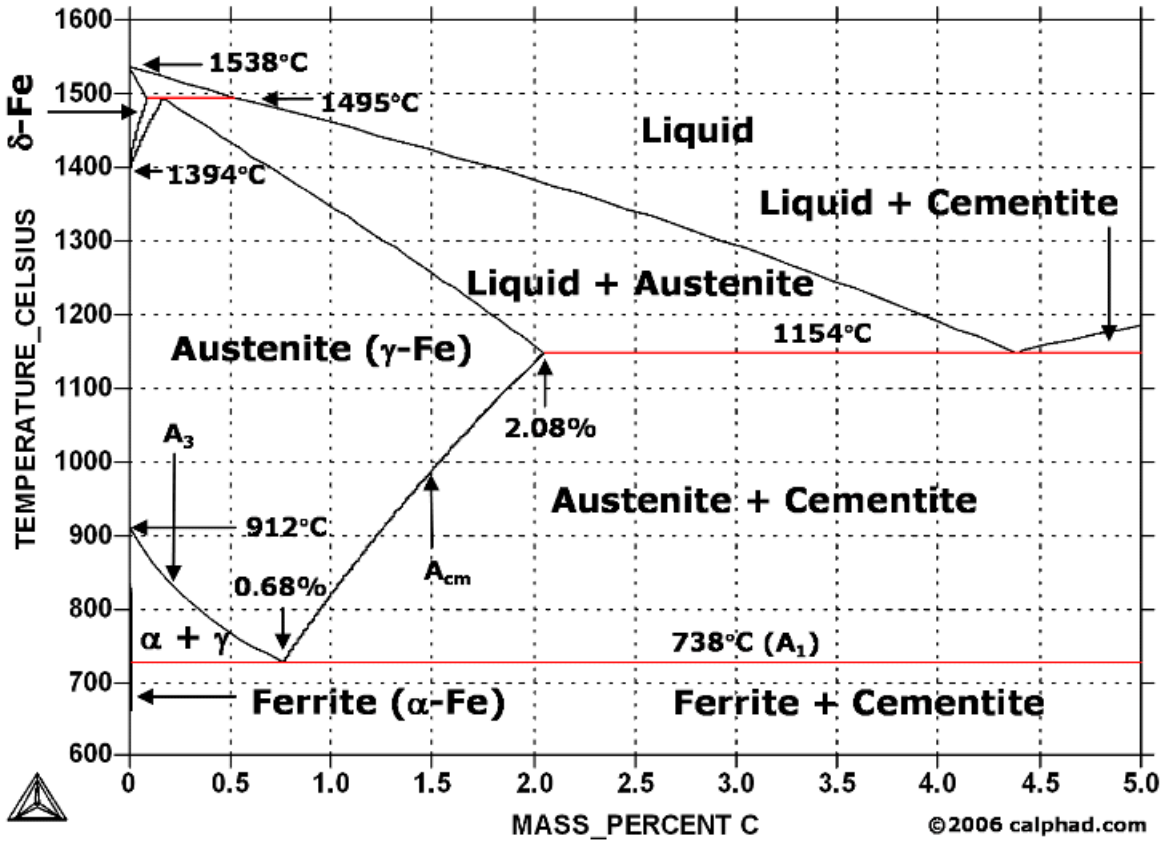

Figure 2.4 Fe-C binary phase diagram showing phase transformation of typical carbon steel during heating [29]**.**

2.2 Surface Coating in AHSS

2.2.1 The need for surface coating on sheet steel

S Steels are subject to environmental attacks during its processing and service cycle. Processes such as the press-hardening can damage the steel. Under high temperature, surface oxidations and decarburization are promoted due to the higher diffusion rate of oxygen into the steel surface and carbon out of the steel surface respectively. Oxidations cause rusting and scaling formation and decarburization cause formation of ferrite layer near the surface, both of which can damage the surface finishing and impact the mechanical performance. An example of surface decarburization is

shown in Fig. 2.5 showing formation of a ferrite phase and lack of martensite due to decarburization. Therefore, surface coatings are necessary to protect the AHSS from oxidation and decarburization.

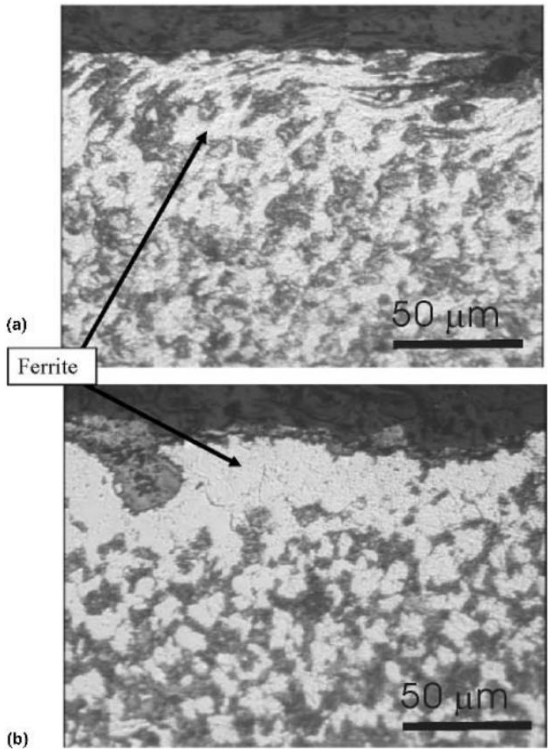

Figure 2.5 a) Before and b) after of surface decarburization in steel and formation of ferrite layer [30]

2.2.2 Protective surface coating on AHSS

Surface coatings are often applied on the steel surface to protect against corrosion and extend their service life by providing a physical barrier and a galvanic protection (in the case of Zn based coating) [11], [31]. Zn, Al, Si, Cr, and Mg are popular elements used in surface coatings depending on the need. Multiple coating methods, such as hot-dipping, electro-galvanizing, and cold spray, can be used based on the application and dimension of the part. For automotive sheet metal, the continuous hot-dip galvanizing is mostly used by the industries due to its high throughput and cost-effectiveness.

2.2.3 Zn-based Coating and Continuous galvanizing line (CGL)

Coatings for automotive sheet metals were mostly applied with a continuous galvanizing process as it is the most cost-effective method [32], [33]. In addition to the physical barrier protection, the Zn-

based coating also serves as a sacrificial coating layer to provide additional protection against oxidation due to its lower potential energy. A typical CGL setup is shown in Fig. 2.6. The coils of steel are welded at the beginning of the line into a single strip. A surface cleaning process with an acid wash and a heat treatment is performed on the strip. Then the cleaned strip is submerged into a molten pool, which is mainly comprised of Zn with traces of Al (0.1%), where a layer of coating forms on the surface, hence "hot-dip". The excess coating is wiped from the strip with an air knife to maintain a consistent coating thickness. Post-dipping heat-treatment can be used to produce the galvannealed (GA) coating. Right after the strip exits the Zn pool, the sheet is being heated up to a temperature of 500~550 °C to promote diffusion between the surface Zn and the steel matrix. With proper annealing, the final GA layer contains three different alloys including Gamma (Γ), Zeta (ζ), and Delta (δ) layers as shown in Fig. 2.7. The Fe content in these three phases is about 10%. The GA coating offers superior resistance to corrosion, improved paintability, and better weldability compared to galvanized Zn coating due to the better charge transfer resistivity with the intermediate layers [34]. In addition, the compression deformability of the Γ and ζ Fe–Zn intermetallics mitigates the detachment of brittle intermetallic coating of galvannealed steels [34].

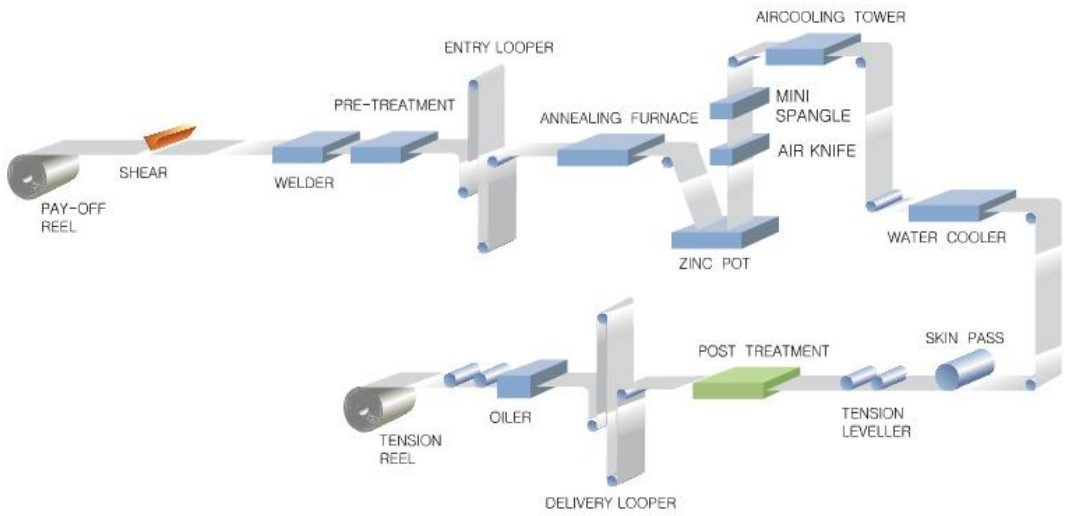

Figure 2.6 A typical continuous galvanizing line set-up [35]

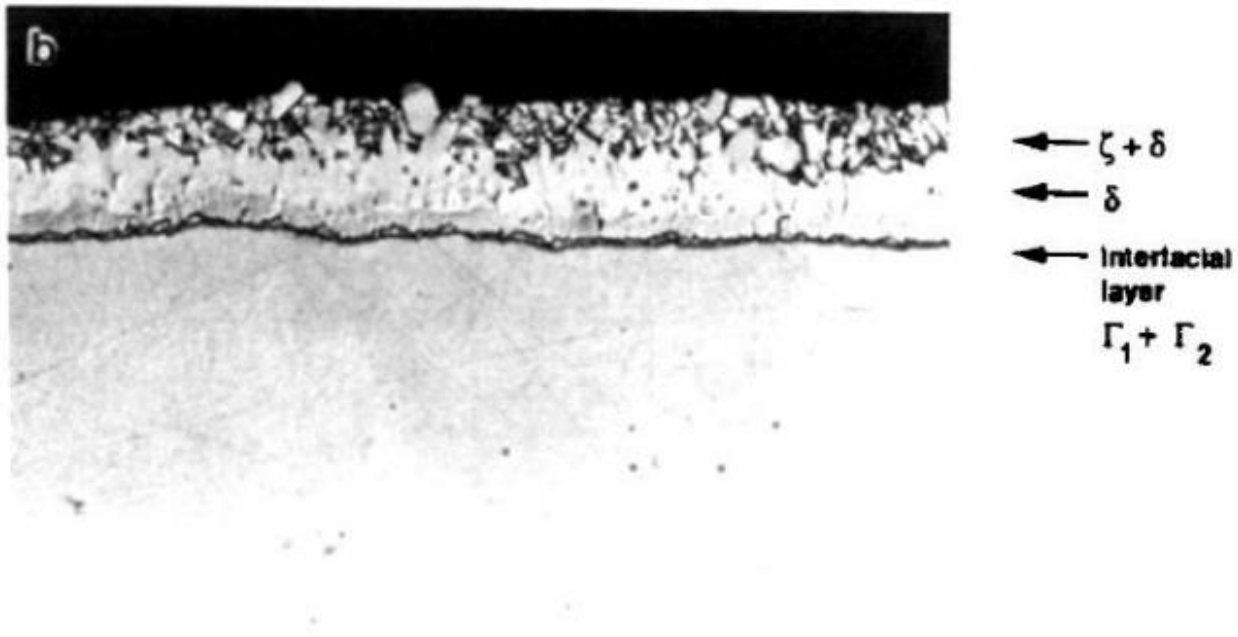

Figure 2.7 Galvannealed Zn coating featuring the different Zn and Al-Fe phases [36]

2.2.4 Characteristics of Aluminum Silicon Coating

Aluminum-silicon coating is another popular method beside Zn-based coating in the sheet metal manufacturing industry to protect the steel against oxidation and decarburization [37], [38]. An Fe-Al diffusion layer form on the steel surface as the result of surface diffusion. An Al_2Fe_5 intermetallic layer forms on the surface of the steel substrate, effectively protect the steel from further reactions (Fig. 2.8). While the AlSi coating provides corrosion resistance to the steel sheet, the use of AlSi can reduce weldability, especially after press-hardening when complex intermetallic compound forms [39], [40]. Therefore, AlSi coatings will not be further studied in this work.

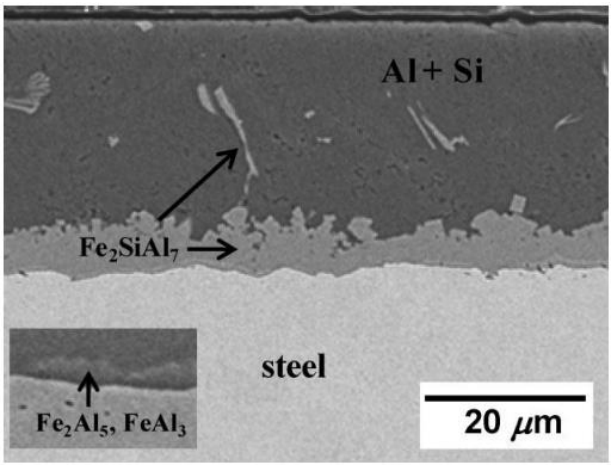

Figure 2.8 Morphology of AlSi coated steel under SEM scan. [41]

2.2.5 Surface Cleaning in Hot-dip Process for Zn Coated Steels

Surface cleanings are necessary to remove contaminant and oxidation from the steel surface to ensure consistent final coating conditions. Coating defects can form when an excessive amount of contaminants is present on the steel surface. Contaminants such as oxides or organic matters can attach to the surface and prevent reactive wetting of the zinc pot to the steel surface (Fig. 2.9) [41], [42]. Coating defects severely reduce the service life of automotive parts and potentially pose a safety hazard due to loss of structural integrity from rust formation. Conventional cleaning methods include acid bath and high-temperature oven baking [43]. These methods effectively clean surface contaminant and organic matters, but they are not effective for cleaning the AHSS due to the high alloying content in the AHSS. In AHSS, Surface oxide forms immediately on the cleaned surface when exposed to the open air environment due to the high alloying content. Thus, special techniques such as selective internal oxidation are required to prevent the formation of surface oxide and to ensure coating consistency.

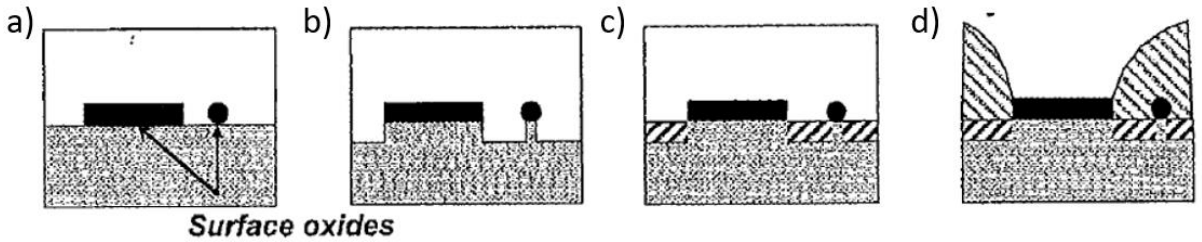

Figure 2.9 Formation of coating defects: a) deposition of surface oxides or contaminants, b) contaminants were not etched, c) lack of Al interlayer in oxide region, and d) reactive wetting resulting bare spot and inclusion of contaminant which promote premature failure. [44]

2.2.6 Selective Internal Oxidation

One difficulty with galvanizing of AHSS is due to its high alloying content. External oxide formation increases the surface energy between the surface and molten Zn pool, which prevent reactive wetting of the molten liquid zinc pool to the steel surface. The selective oxidation is a process used to improve the reactive wetting of the steel surface to the zinc pool by reducing the formation of surface oxides [45]. In selective oxidation, the steel substrate is annealed in a controlled low dew point environment to form a sub-surface internal oxide (Fig. 2.10) [45]. Presence of this internal oxide layer prevents further formation of external oxide which increases the wettability.

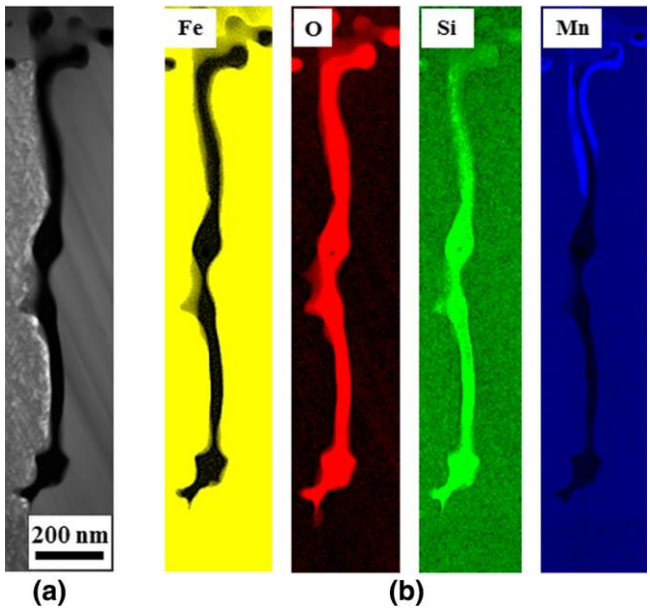

Figure 2.10 a) SEM image and b) elemental analysis of internal oxidation showing the concentration of Fe, O, Si, and Mn content near internal oxide. [45]

2.3 Resistance spot welding (RSW)

2.3.1 Overview of RSW

Resistance spot welding is a fusion welding technique to joining sheet metals developed in the late 1800s by Elihu Thomson from his patent on Apparatus for Electric Welding in 1886 [46]. The first spot welding machine was invented in 1906 and was used in the automotive industry in the 1930s. This technique is still used in today's automotive manufacturing due to its efficiency and speed [47]. RSW is a fusion welding process using the concept of joule heating to melt and connect metal parts. The metal parts to be joined are held together by a pair of copper electrodes. A high current is passed through the metal parts where the electrical resistance generates the heat required to melting the interface. The heat generated (Q) in the welding process can be expressed in the following equation, where R is the resistance of the faying surface, t is the time, and I is the current (Eqn. 2.1). As the resistance is dependent on time during the welding, an integral form can be used to compute the total heat input into the weld region for the RSW process (Eqn. 2.2).

Equation 2.1 $Q = I^2Rt$

Equation 2.2 $Q_{Total} = \int I^2Rdt$

As the material reaches its melting temperature, a molten pool of liquid metal forms at the faying surface. The current is then halted at the end of the RSW process, and the water-cooled electrode cools the molten pool to form a solid joint. This joint is referred to as the weld nugget due to its final shape. A schematic of the resistance spot welding setup is shown in Fig. 2.11. With the simple setup of the RSW and its short cycle time of less than 500 ms, the RSW process is popular within the automotive industry with 3000 to 6000 welds performed per commercial vehicles [48]

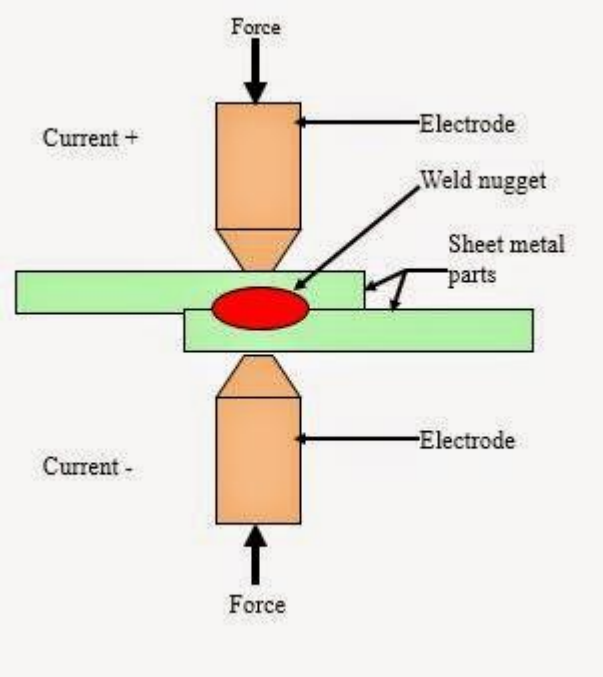

2.11 A typical resistance spot welding setup showing two metal sheets being welded in a lap condition [49]

2.3.2 Process parameter in RSW

Different process parameters, also referred to as weld parameters, can be used to control the welding process. As welding energy is generated by resistive heating, the different components from the Joule heating equation, such as welding current and time, are the most basic parameters that can be directly controlled by changing the weld sequence [50]. Based on Eqn. 2.1, increasing welding current or time will increase the heat generated during the welding cycle.

The last component of the Eqn. 2.1, the electrical resistance, is a combination of the material bulk resistance and the resistance associated with the surface contacts [51]–[54]. The surface resistance is dependent on the contact condition between the different contact surfaces, which can be controlled by the electrode face size and pressure. Larger electrode face size allows a higher contact surface, reducing the electric resistance between the two surfaces. Higher electrode force increase in contact surface area as the asperities are compressed, reducing the surface contact resistance and decreasing the heat generation [55]. The bulk resistance is mainly governed by the intrinsic physical properties of the material, which is not an adjustable parameter, where changes in the bulk resistance during the weld cycle is associated with the material temperature and electrode indentation.

2.3.3 Process Window and Weld Lobe

A processing window for the RSW can be measured, which indicates the range of parameters that will result in a sound weld. Welding with parameters on the left side of the process window will result in an undersized nugget (the criteria for undersized nugget can be found in section 2.3.5) and expulsion (on the right side of the curve) where molten metal escape the joint because too much heat is being introduced [56]. Both undersized nugget and expulsion are detrimental to the weld performance and unacceptable by the AWS D8.9 welding standards [57].

When measuring the process window, the welding current and time are varied while the other parameters such as electrode size and pressure are kept constant. To determine the weld process window, welds were made at each current increment to determine if the current falls within the limit, defined by the minimum weld diameter and the occurrence of expulsion. This process is repeated over at different weld times (Fig. 2.12a) and can be translated into a process window (Fig. 2.12b). This process window is often shaped in the form of a lobe, therefore commonly known as the welding lobe [48].

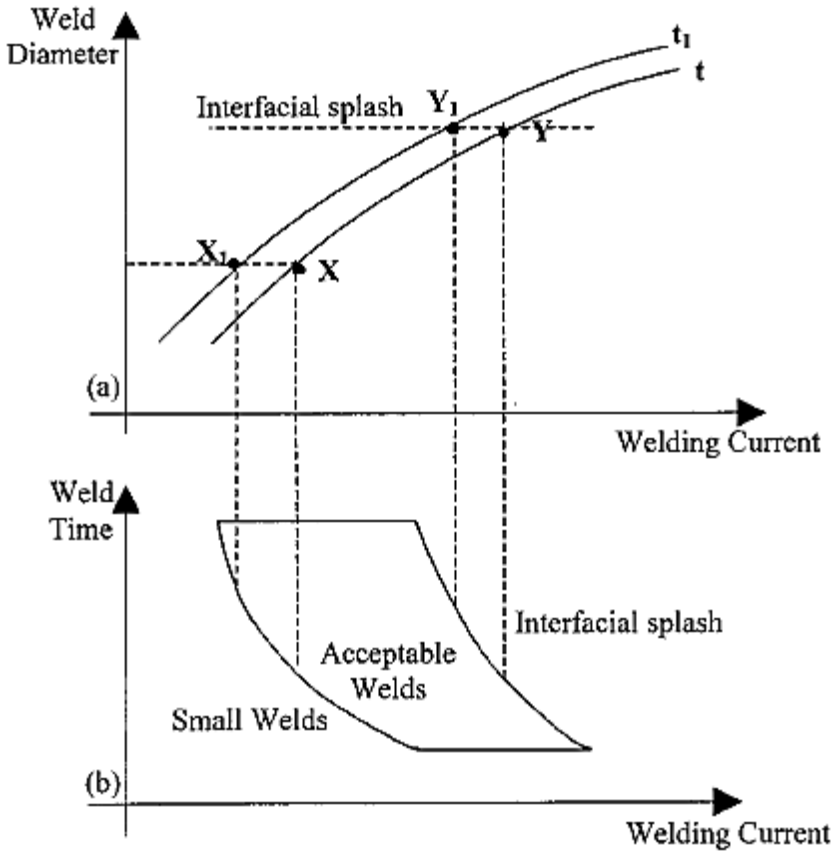

Figure 2.12 a) Processing windows measured at different weld time where minimum nugget size is labeled as X and expulsion condition labeled as Yand b) weld lobe in resistance spot welding [58]

2.3.4 Effect of Nugget Size on RSW failure mode

The mechanical performance of the welded joints was measured using the tensile lap shear test. Typical failure modes observed in a lap shear test includes the button pullout, partial pullout, and interfacial failure [59]–[61]. In button pullout, fracture occurs in the base material or the HAZ, and the propagation path goes around the nugget (Fig. 2.13a). This failure mode is preferred because it can absorb a higher amount of energy during a crash scenario [59]. Interfacial failure is characterized by the fracture from the previous faying surface of the joint (Fig. 2.13b). This fracture mode is brittle and absorbs less energy compared to the button pullout failure. This failure mode is unacceptable by the automotive industry as it can pose safety concerns [57]. Partial button pullout is a combination of the two failure modes mentioned above. It provides better crashworthiness than interfacial failure, however, it is not the preferred mode of failure.

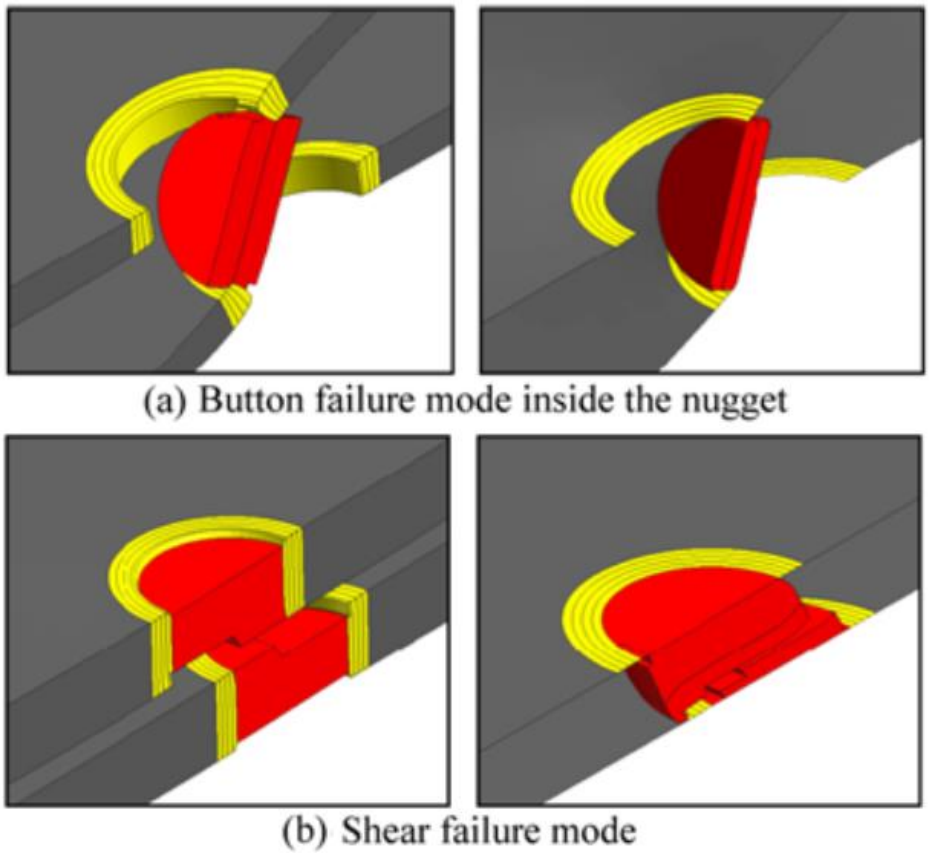

Figure 2.13 Different failure modes in lap shear test of RSW joints featuring a) nugget pull out and b) interfacial failure. [61]

2.3.5 Determination of Minimum Nugget Size

Several studies have shown that the nugget size dictates the failure mode and load-bearing capacity of an RSW joint [59], [62], [63]. Therefore, the nugget size was used to estimate the mechanical strength of the welded joint, where a minimum nugget size is determined to reflect the quality of a weld. The minimum nugget size is described using the equation c*sqrt (t) where t depicts the thickness of the material. The c-value of 4.0 is suggested by the AWS D8.9 standard [57]. However, other studies have suggested a range from 3.0 to 5.0 dependent on the strength of the material where weaker material such as mild steel requires smaller nugget and tougher material such as the PHS requires a larger nugget [59].

2.3.6 Heat Affected Zone in RSW

In any fusion welding process, the surrounding material is subjected to a temperature change due to the temperature field that forms near the weld. A typical resistance spot welding can be separated into three regions, the fusion zone (FZ), heat-affected zone (HAZ), and the base metal (BM), depending on the local peak temperature during welding (Fig. 2.14). The FZ is located at the center where the solidified molten metal joins the two pieces of material together [64]. In RSW, the FZ is often referred to as the nugget due to its oval shape. A martensitic microstructure is often observed in this region due to its high cooling rate in the welding schedule. The heat affected zone (HAZ) is located right next to the FZ. The HAZ is often further separated into three sub-regions: upper-critical (UC), inter-critical (IC), and subcritical (SC). The different HAZ regions are characterized according to their peak temperature reached in the respective regions. The UC-HAZ is located closest to the fusion zone where the peak temperature reached above the A_{C3} temperature. In the UCHAZ, austenitic structures are formed during the welding process. In the IC-HAZ region, the peak temperature during welding is between the A_{C1} and the A_{C3} temperature. Partial austenitization is reached in this region while the rest of the steel remains in the original phase while being tempered. In the SC-HAZ, the temperature remains below the A_{C1} temperature. The temperature is not high enough to allow austenitization to form, but enough to enable tempering of the existing structure. In the base metal section, the steel fully retains its original microstructure unaffected from the welding process.

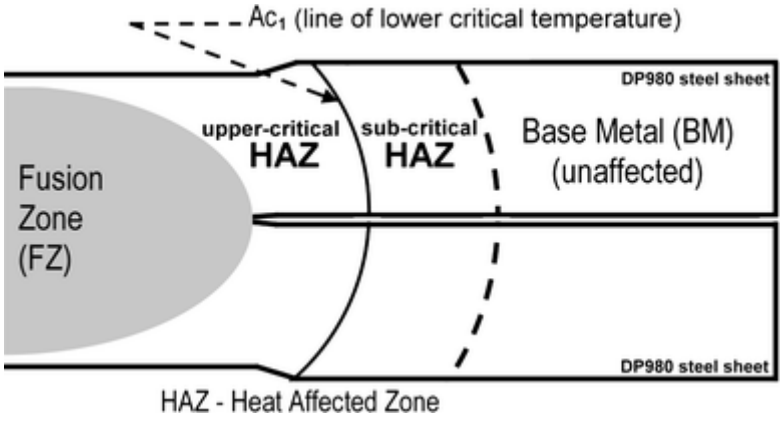

Figure 2.14 Illustration of the different zone in a resistance spot welding featuring the fusion zone (FZ), upper-critical heat affected zone UC-HAZ, sub-critical heat affect zone (SC-HAZ), and base metal (BM) [65]

2.3.7 Nugget Size Measurement

Destructive testing methods

Destructive characterization methods are often used to accurately measure the nugget size [66]. Chisel and peel tests are the basic methods used to measure the nugget size. Chisel test involves inserting a chisel between the bonded sheets to open the weld to inspect the nugget (Fig. 2.15a). The nugget dimension can be measured from the fractured surface. The peel test uses a specialized tool to peel one sheet away while the other sheet is anchored to a platform (Fig. 2.15b). As the top sheet is being peeled away, the weld nugget is revealed either in the form of pulled-out nugget or interfacial failure.

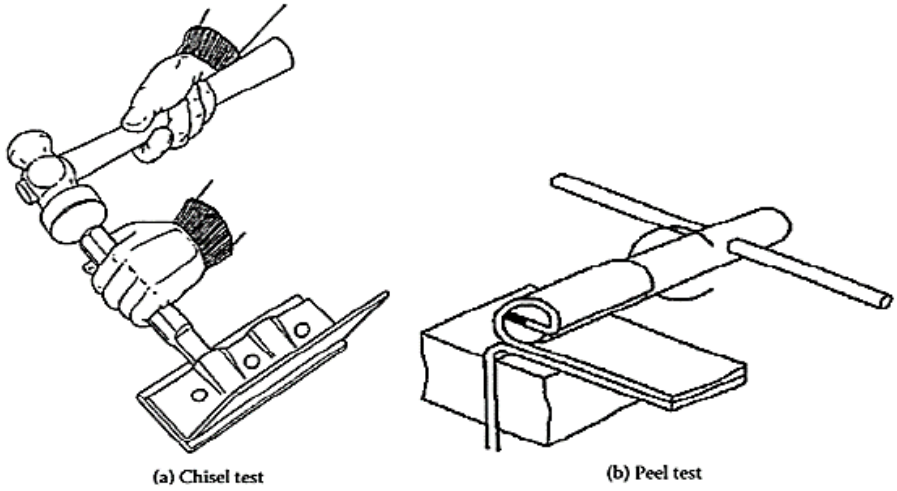

Figure 2.15 a) Chisel test and b) peel test to verify nugget sizes of a resistance spot welding joint [66]

Non-destructive Measuring Methods

While the above methods can measure the strength of the weld, their destructive nature does not allow these tests to be performed on every joint. To measure the effectiveness of all the joints, non-destructive methods such as x-ray scan, ultrasonic scan, or magnetic flux testing should be used [67]. Currently, the ultrasonic scan is the most accurate testing method for RSW joint [68]. Ultrasonic waves are being used to scan the weld surface and the feedback signal can be directly correlated to the nugget size with great accuracy. However, ultrasonic testing requires the weld surface to be flat which add additional preparation steps into the testing procedure. The complicated and lengthy procedure slows down the RSW process. In addition, implementation of an ultrasonic tester into the

existing system requires a significant capital investment which can hinder their introduction. Therefore, NDT methods are not widely adopted by the automotive industry.

2.3.8 Dynamic Resistance Curve

During the welding cycle the resistance of the joint with a change in response to changes in the material temperature and surface roughness, this is known as the dynamic resistance. Dynamic resistance curves can be used to monitor weld development as an in-situ method. Measurement of dynamic resistance was first used in the 1970s [51], [69]. Static resistance measurements were commonly used to characterize a resistance spot weld before the notion of dynamic resistance. However, static resistance can only reflect the electrical resistance at the beginning of the welding cycle. Weld development is not taken into consideration which makes static resistance measurement incapable of fully representing the RSW process. Realizing the shortcomings of static resistance, researchers started recording the resistance variation during the welding process [70]–[72]. With advancements in dynamic resistance measurement, a more in-depth weld development has been observed. Relationship between weld development and dynamic resistance has been proposed to reflect the weld evolution during the weld cycle [72].

Uncoated steel

A typical RSW dynamic resistance curve for the uncoated steel was recorded by Dickinson et al. is illustrated (Fig. 2.16) [72]. The dynamic resistance curve has been separated into five different regions based on the development of the weld (Fig 2.16).

Stage I: Quasi-static and surface breakdown

At the beginning of stage I, a resistance value similar to the static resistance is measured. The resistance value starts to decrease in stage I as surface contaminants layers start to break down.

Stage II: Softening and Reduction of Asperities

As the weld process proceeds, the faying surface begins to change. Softening of asperity causes the dynamic resistance to decrease as contact surface increases. While heat starts to build up in the faying surface causing the resistance to increase, its effect cannot be observed as it is masked by the asperity softening.

Stage III: Bulk Heating

As the softening of surface asperity is completed, bulk heat becomes the only factor to influence the dynamic resistance. As the material is heated, the material resistance starts to increase, resulting in the overall increase of the dynamic resistance.

Stage IV: Melting of Faying Surface

As the temperature at the faying surface reaches the melting temperature, surface melting occurs which indicates the beginning of region IV. As liquid contact forms between the two workpieces, the contact resistance starts to drop, which lead to the formation of the beta peak.

Stage V: Nugget Growth

After the faying surface is fully melted, the nugget growth stage begins. The growth of nugget results in a continuous reduction of dynamic resistance due to the increased contact area due to the mechanical collapse. If too much heat is being introduced to the weld samples, expulsion occurs because the electrode is unable to hold the nugget. Expulsion is characterized as molten metal ejections from the nugget. A sudden drop of resistance is observed due to the formation of a shunting path from the ejected molten metal.

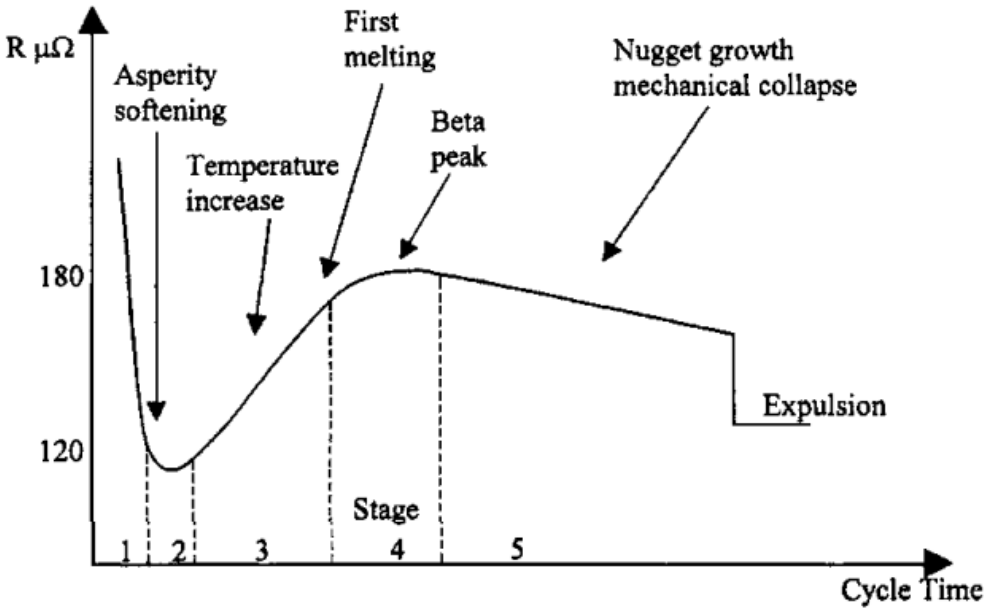

Figure 2.16 Dynamic resistance development in conventional uncoated steel featuring the different stages of the welding cycle. [58], [72]

Coated steel

Based on the result of the uncoated steel, William et al. have furthered the understanding of dynamic resistance curve to the coated steel [48]. In coated steel, the dynamic resistance behavior has more complications due to the presence of the coating layer. The coating usually has a different mechanical and thermal properties compared to the base material. As a result, more stages are present

compared to the original 5 stages in the uncoated condition as shown in Fig. 2.17. Compared to the uncoated condition, the coated steel has a deeper alpha trough between stage 3 and 4, which is associated with the additional effect from the melting of the zinc layer. In addition, new troughs were observed for the breakdown of insulating film at the end of stage 1, and the formation of zinc bond at the end of stage 5. After stage 5, the remaining development of the dynamic curve is similar to what was observed in the uncoated case.

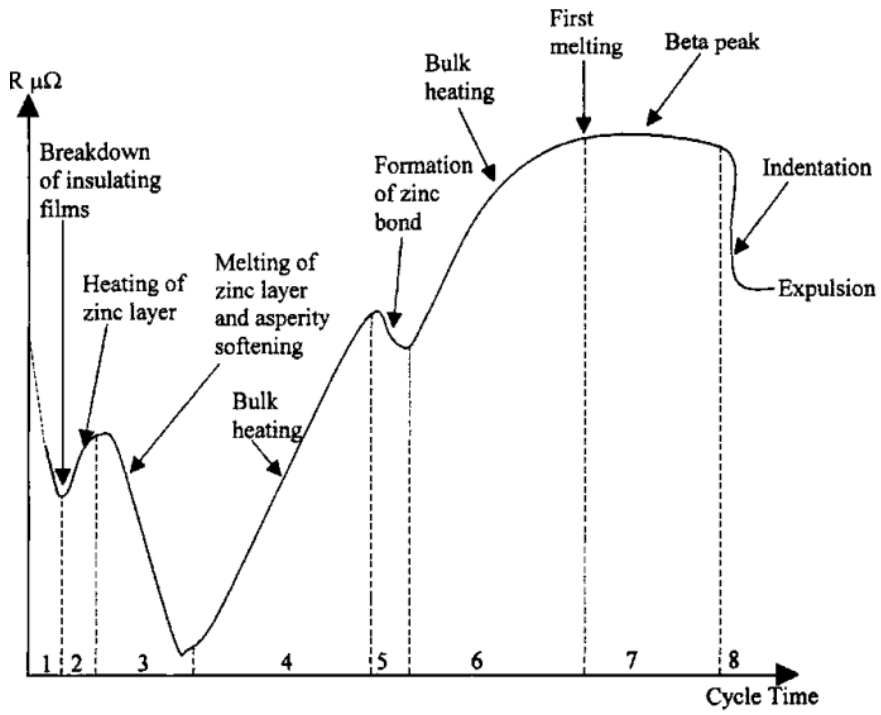

Figure 2.17 Dynamic curve of galvanized Zn-coated steel. [58], [73]

2.4 Possible Variations in surface conditions of AHSS and their impact on the RSW process

Variations in the surface layer condition, such as oxidation or coating layers, may occur as a result of changes in materials or processing parameters. Such changes in surface conditions impact the RSW process by changing the resistive behavior of the material. As the weldability and weld lobe may be impacted by changes in surface condition, it is important to understand the different surface effects. This section will discuss a few variations in surface related conditions and their effect on the RSW process.

2.4.1 Effect of Surface Oxidation Condition

Surface oxidation may occur on the unprotected steel surface when it is exposed to oxygen. Variations in surface oxidation can be introduced from a difference in the oxygen content and exposure time. Crinon et al. have shown that with increasing surface oxidation, the contact resistance between the sheets increased (Fig. 2.18) [52]. As the degree of oxidation changes the resistance profile, the welding current must be adjusted to ensure productions of sound welds.

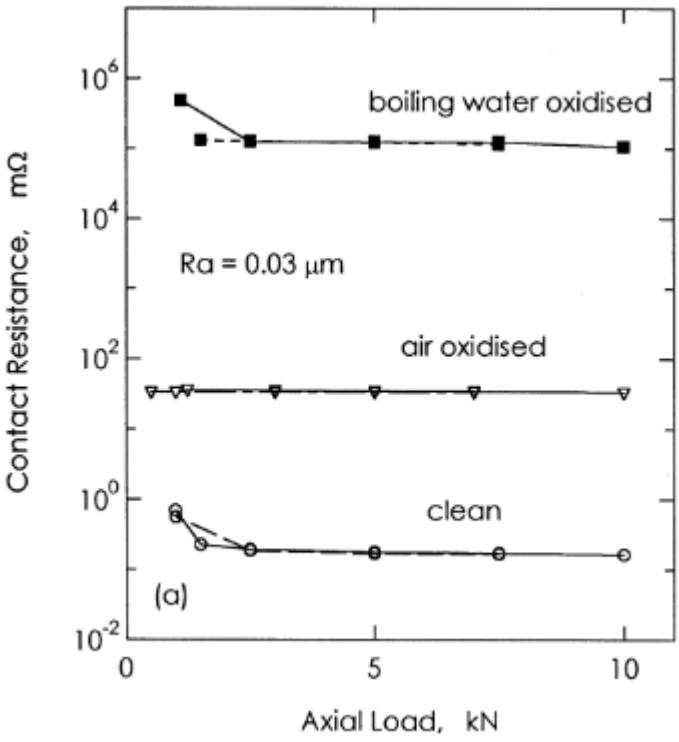

Figure 2.18 Contact resistance-force curves showing the effect of oxidation treatment on the faying surface contact resistance. [52]

2.4.2 Effect of Selective Internal Oxidation

As mentioned in section 2.2.6, selective internal oxidation is necessary to ensure a uniform coating layer in some of the AHSS (mainly CMnSi steels). Annealing time can differ based on the steel chemistry. A different oxide morphology is observed when a variation in annealing time is introduced (Fig. 2.19). As variations in the external oxide have shown an impact on the RSW process, the effect of the internal oxides on RSW must be verified to ensure weld consistency [52]. However, no literature has reported the relationship between change in the internal oxide condition and the

RSW process. Additional work is required to understand the effect of internal oxide on the RSW process.

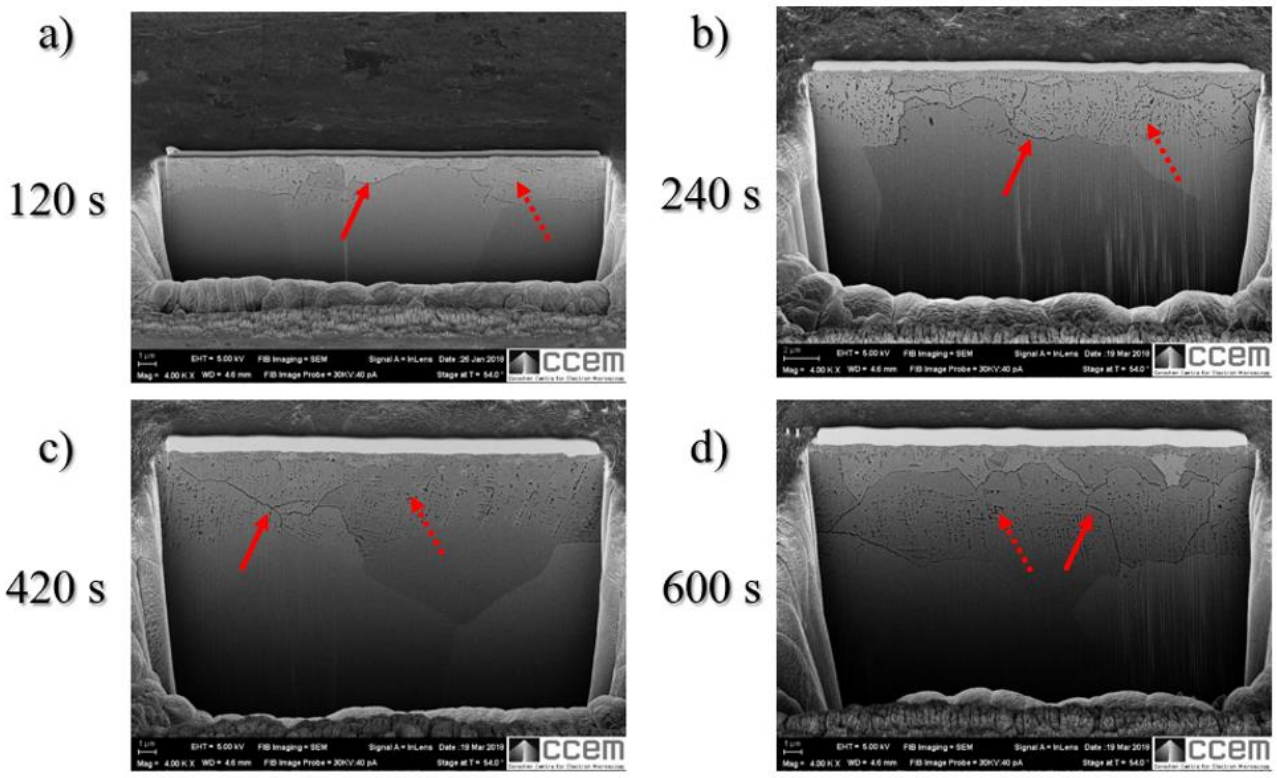

Figure 2.19 Evolution of subsurface oxidation (intergranular oxides labeled with solid arrows and intragranular oxides labeled with dashed arrows) at different annealing time of a) 120 s, b) 240 s, c) 420 s, and d) 600 s. [74]

2.4.3 Effect of Surface Coating Types

As mentioned in section 2.2.2, different types of protective surface coating are available for the AHSS. In the case of PHS, Al-Si and Zn based coatings are both commercially available. Osayande et al. have shown that for the heat-treated PHS, the two coating types require different welding current due to their difference in electrical resistive behavior (Fig. 2.20) [11]. Therefore, changes in surface coating type must be considered when setting up RSW welding parameters.

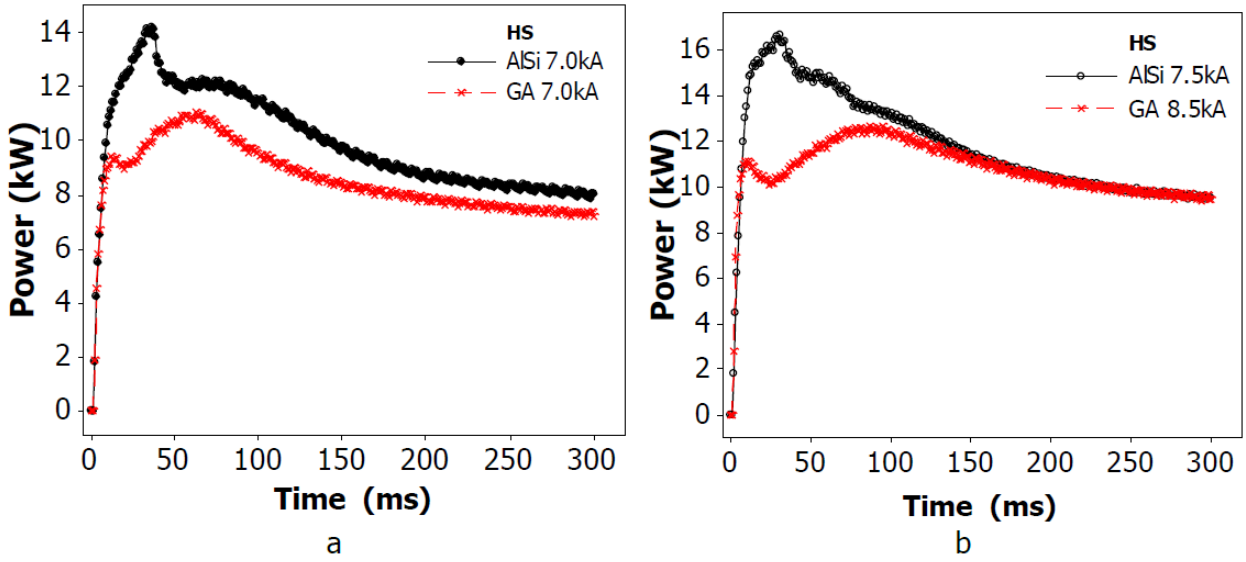

Figure 2.20 Comparing heating rate required for heat-treated AlSi and GA for generating equivalent sized nuggets: (a) 5.6 mm nugget and (b) 5.9 mm nugget. [11]

2.4.4 Effect of Zn Diffusion Layer from Heat-treatment of PHS

High-temperature heat treatments were often necessary to achieve certain properties in the steel sheets such as in the heat-treatment of PHS. Under high temperature, Zn from the coating layer inter-diffuse into the Fe substrate [75]. According to Fick's law of diffusion, the diffusion process and the final distribution of Zn content are dependent on the initial Zn content (concentration of diffusant), the heat-treatment temperature, and the heat-treatment time (diffusion time) (Fig. 2.21) [76]. Change in depth and composition of the Zn diffusion layer has the potential of changing the surface resistance profile; however, there is a lack of literature in the effect of Zn diffusion layer. Further studies are required to understand the effect of variation in the Zn diffusion layer on the RSW process.

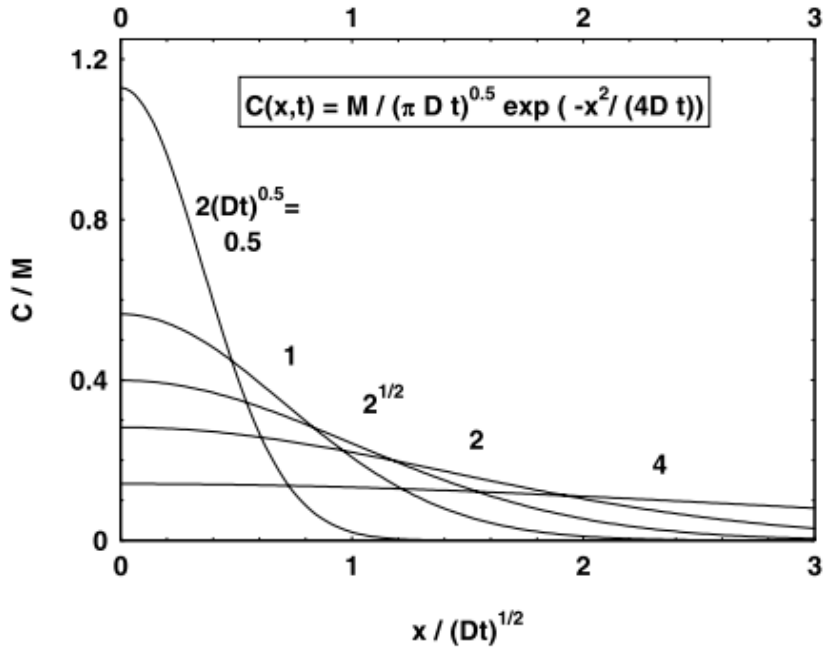

Figure 2.21 Diffusion mechanism showing the effect of time over the diffusion length and distribution of atoms. [77]

Chapter 3 Materials and Experimental Methods

3.1 Overview

Two sets of separate experiments were designed to study both internal oxidation and zinc coating diffusion effects on the resistance spot welding process of advanced high strength steel. Two different types of materials and preparation methods have been used to evaluate the above effects. In this chapter, the preparation methods are listed separately for each study. The resistance welding technique, analytical methods for microstructure and nugget size measurement were similar for both studies.

3.2 Sample Preparation Methods

3.2.1 Internal Oxide Samples with CMnSi Steel

The advanced high strength steel with C, Mn and Si contents as main alloying components, provided by the International Zinc Association, was used for the internal oxidation study. The detailed chemical composition for each grade is listed in table 3.1. Varied Si content was used to evaluate the effect of alloying content. These materials were received in as-rolled condition with no surface treatment, further heat treatment was completed to introduce internal oxidation.

Table 3.1 Chemical Alloying Composition of CMnSi Steels Used for Internal Oxidation Weldability Study (wt. %)

Grade	C	Mn	Si	P	S	Al	Cr	Ti	B	Fe
CMnSi 2/0.7	0.10	1.96	0.70	N/A	0.002	0.05	N/A	0.010	N/A	Bal.
CMnSi 2/1.7	0.10	2.03	1.76	N/A	0.002	0.04	N/A	0.010	N/A	Bal.

The selective internal oxidation process was completed by Prof. McDermid's team at McMaster University. Controlled annealing was used to simulate the continuous galvanizing process in steel

manufacturing to promote selective internal oxides under the steel's surface. The McMaster Galvanizing Simulator (MGS), shown in Fig. 3.1 a, was used to perform the annealing process.

The MGS can simulate the industrial hot-dip galvanizing line. The MGS consists of an infrared heating chamber with environmental dew point control, N_2 gas wiping, and molten zinc bath. The hot-dip galvanizing step was not performed to avoid deposition of Zn onto the sheet surface, as the Zn coating layer will add a second effect which could mask the effect of internal oxidation. The heating cycle used for the selective internal oxidation is shown in Fig. 3.1b and annealing conditions in table 3.3.

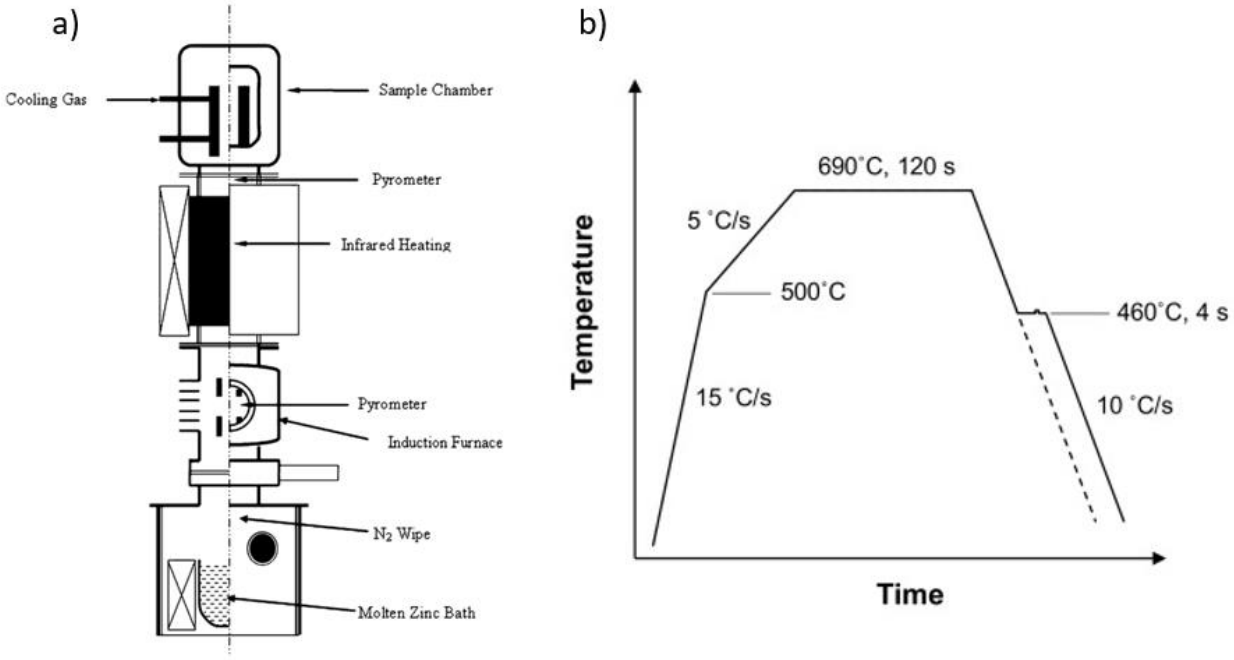

Figure 3.1 a) Schematic of the McMaster Galvanizing Simulator (MGS) and b) the annealing heating cycle used for selective oxidation with a hold time at 690 °C for selective internal oxidation and 460 °C for hot-dip galvanizing (hot-dip galvanizing is not performed for samples used in this thesis, please refer to the dotted line for the annealing only condition).

Table 3.2 Annealing Condition for CMnSi Steels

Peak Temperature Holding Time	Annealing Temperature	Dew point	Atmosphere
0/240/420 seconds	805 °C	-5 °C	N_2-5H_2 vol%

3.2.2 Zn Diffusion Samples with Press-hardening Steel

Industrial 22MnB5 press-hardening steels (PHS) with a thickness of 2mm were provided by ArcelorMittal Dofasco to evaluate the effect of changes in Zn coating on the resistance welding process. The detailed chemical composition of the material can be found in table 3.3. The as-received PHS was in a non-hardened ferrite/perlite microstructure. Steel sheets were sheared into 200mm by 200mm squares to facilitate the press-hardening process.

Table 3.3 Chemical Composition of the 22MnB5 Press-Hardening Steel (wt%)

C	Mn	Si	P	S	Al	Cr	Ti	B	Fe
0.23	1.19	0.25	0.016	0.002	0.05	0.20	0.031	0.003	Bal.

To complete the press-hardening process, the PHS must undergo an austenitization process and be quenched. Heat treatment was conducted in an oven with six sets of heating elements to ensure uniform heating. The six sets of heating elements are distributed in two layers, three on the top of the oven and three on the bottom. The three heating elements are located at the front, middle, and rear portion of the furnace, each section equipped with their own thermocouple for temperature feedback. Three heat-treatment times of 4, 7, and 10 minutes were used to investigate the effect of heat treatment time on Zn diffusion. Similarly, two different holding temperatures of 860 and 900 °C were used to examine the effect of heating. An automatic transfer system transfers the sheets from the oven to the press to ensure consistency in the press-hardening process (Fig. 3.2). A Macrodyne hydraulic press was used for the quenching process (Fig. 3.2). Water-cooled stainless-steel flat die was used to provide a high cooling rate to ensure martensitic transformation during the press-hardening process. Pressing parameters are listed in table 3.2.

Table 3.4 Heating and Press-hardening Parameters for the PHS Steel

Heating Temperature	Heating Time	Press Force	Quench Time	Die Temperature
860°C	4min / 7min / 10min	10 T	30 sec	< 40°C
900°C	4min / 7min / 10min	10 T	30 sec	< 40°C

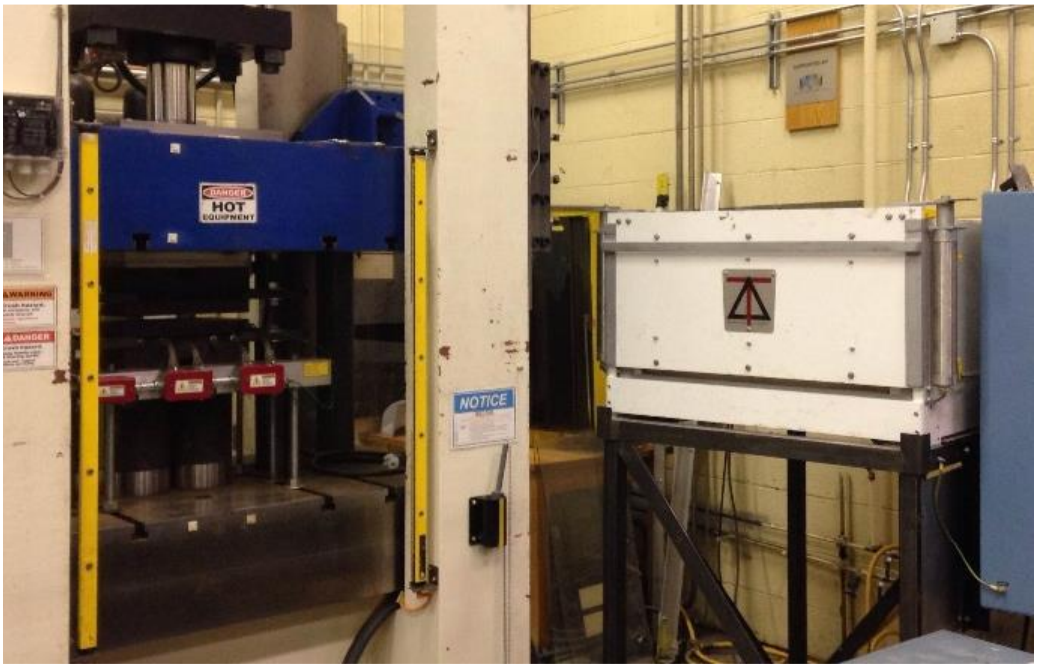

Figure 3.2 Macrodyne press with the automatic oven-transfer system used for the press-hardening operation

3.2.3 Welding Samples Size

Materials were cut into smaller coupons for welding experiments. Mechanical shearing was used in the case of CMnSi steel, and waterjet cutting in the case of PHS. Samples were prepared into coupons with a size of 25mm x 25 mm for the metallurgical test and 25 mm x 100 mm with its length parallel to the rolling direction for the lap shear test. The chosen sample dimension was smaller than recommended by the AWS D8.9 standard due to limited material availability [57].

3.3 Resistance Spot Welding

3.3.1 RSW Equipment

Resistance spot welding was conducted using two medium-frequency direct current (MFDC) welding machines. One of the welding machines was pedestal mounted (Fig. 3.3a) and other was a robot mounted transformer gun (Fig. 3.3b). The pedestal welder provides better consistency due to its stiffness, and the robot offers more flexibility in control and automation. The two welders were equipped with the same weld controller model (Bosch Rexroth) to ensure consistency. Both welders were capable of measuring the real-time welding current, voltage, and resistance with a data

acquisition system connected to the Rexroth® controller. A schematic of the data acquisition setup was illustrated in Fig. 3.4. Voltage measurement was completed across the electrodes. Welding current was measured around the secondary loop with a Rogowski coil placed around the electrode shank. With the voltage and current data, real-time resistance can be calculated across the entire weld cycle.

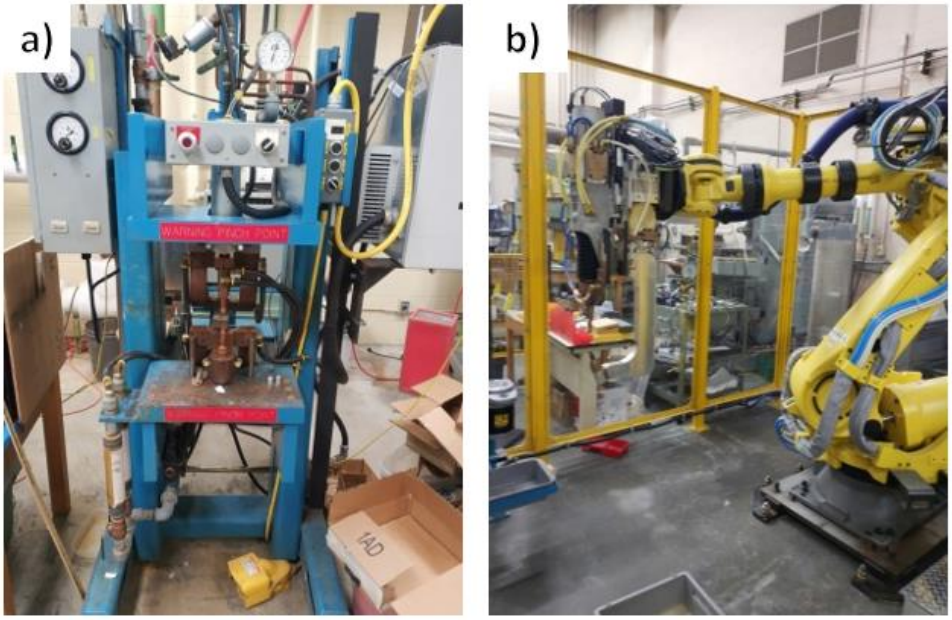

Figure 3.3 Resistance spot welder on a) pedestal base and b) robot arm.

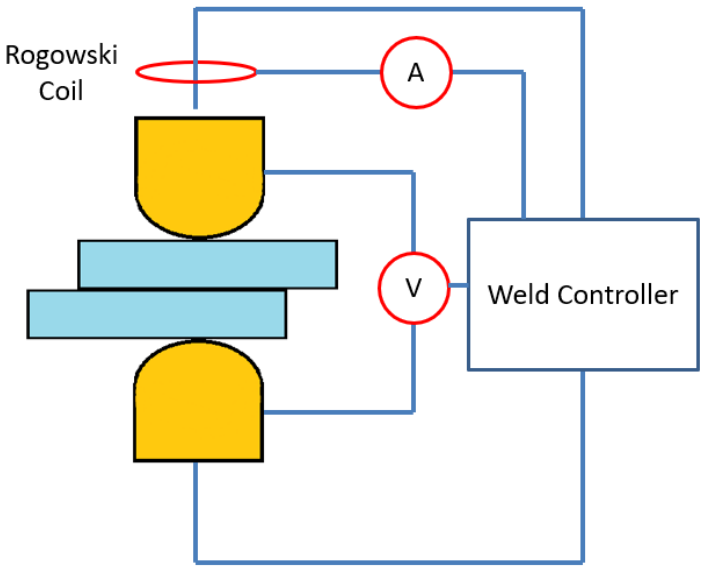

Figure 3.4 Schematic of the data acquisition system

3.3.2 Welding Parameters

Welding parameters were selected from the AWS D8.9 welding standard for group 4 steel listed in Table 3.5 [57]. Welding time was converted from 60 Hz cycle to milliseconds and rounded to the closest millisecond. RWMA CLASS II copper female electrodes with dome-shaped geometry (Type B – body size of 16mm) were used to reflect the industry practice. The dressed face diameter of the electrodes varies from 6-8mm dependent on the thickness of the material based on the AWS standard D8.9 [57].

Table 3.5 Welding Schedule Suggested by AWS D8.9 Standard for Group 4 Steels [57]

Sheet Thickness (mm)	Electrode				Weld Time[d] (cy)	Short Hold Time[e] (cy)	Long Hold Time[e] (cy)	Welding Rate[f] (w/min.)
	Type No.[b]	Dressed Face Diameter (mm)	Force (kN)[c]	Cooling (l/min.)				
0.60–0.69	1	4.5	2.1	4	12	5	90	25
0.70–0.79	2	5	2.6	4	13	5	90	25
0.80–0.89	2	5	2.9	4	14	5	90	25
0.90–1.09	3	6	3.6	4	15	5	90	20
1.10–1.29	3	6	4.0	4	16	5	90	20
1.30–1.49	4	7	4.9	6	10-2-10	10	90	15
1.50–1.69	4	7	5.5	6	12-2-12	10	90	15
1.70–1.89	5	8	6.5	6	9-2-9-2-9	10	90	15
1.90–2.09	5	8	7.2	6	10-2-10-2-10	10	90	15
2.10–2.49	6	9	8.3	6	9-2-9-2-9-2-9	10	90	15
2.50–3.00	6	9	9.1	6	10-2-10-2-10-2-10	10	90	15

3.3.3 Weld Size Measurement

The nugget size was measured to assess the weld quality. Destructive testing methods such as peel test or lap shear were used to reveal the nugget for the CMnSi samples. As the weld nugget was pulled out, the nugget size can be directly measured using a caliper or stereo optical microscope as shown in Fig. 3.5a. In materials with higher base material strength such as PHS, failure occurred in the HAZ or base material. The button pullout method (such as shear or peel testing) was no longer accurate as it included parts of the HAZ region. Cross-section method was used to measure the nugget size for better accuracy compared to the measurement of a pulled-out nugget. To measure the weld using the cross-section method, the weld joint was cut from the center, and the cross-section was etched using the sample preparation method mentioned in section 3.4.1 to reveal the solidified nugget where its dimension can be measured as shown in Fig. 3.5b.

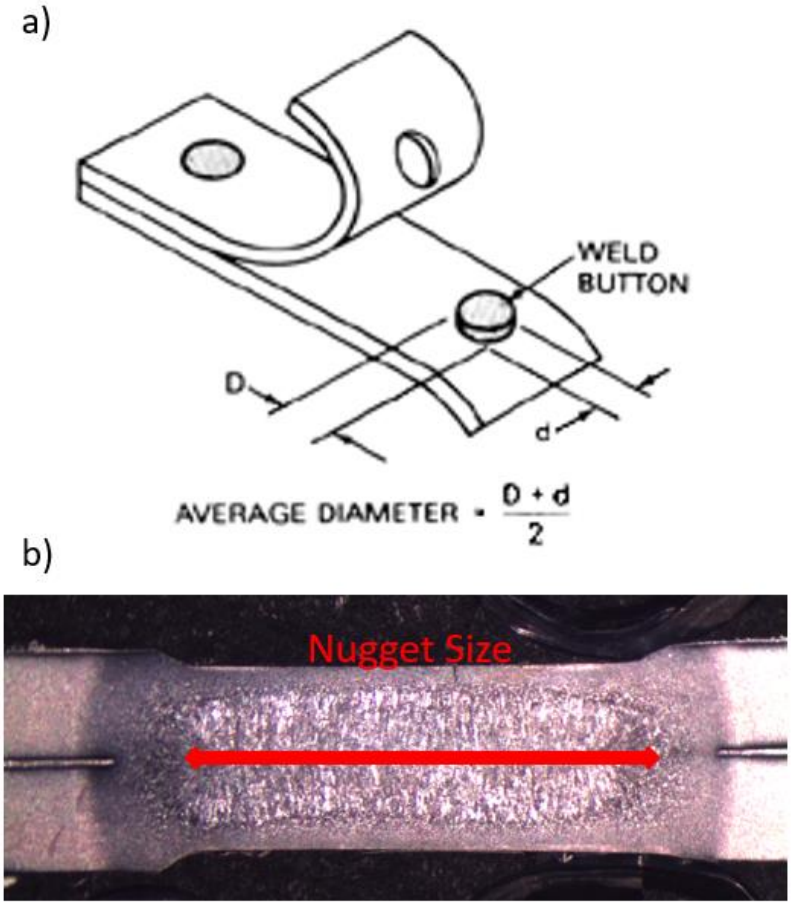

Figure 3.5 RSW nugget size measurement from a) AWS C1.1 recommended practice and b) the cross-section method

3.3.4 Interrupted Testing

Interrupted tests were used to observe the surface evolution and nugget growth at the early stage of the RSW process. In an interrupted test, samples were welded with a reduced welding time to allow observation of the surface condition in the early stage. The weld time was tested with an increment of 10 ms until a solid nugget form. Additional interruptions were performed to observe surface conditions where the dynamic resistance curve has distinct features. Chisel test was used to expose the weld surface condition as the nugget formation is in progress.

3.3.5 Calculation of Heat Input into the Weld Region

The heat input into the weld can be estimated using total energy generated from resistive heating throughout the welding process. The energy generated at each point can be calculated using Joule's

equation (Eqn. 2.1) with measured dynamic resistance. Therefore, the overall heat generated from the RSW process is the summation of all instantaneous heat generated as shown in Eqn. 2.2.

3.4 Metallographic Characterization

3.4.1 Sample Preparation

Samples were cross-sectioned using a cut-off wheel with continuous application of coolant. Cross-sectioned samples were mounted in conductive PolyFast® mounting compound for SEM imaging, and in non-conductive MultiFast® mounting compound for optical imaging and hardness measurement. Metal clips were used to prevent sample tilting during the mounting process. Grinding was completed using SiO grinding paper with incremental grit number (180, 320, 400, 600, 800, and 1200 grits). The samples were then polished to a mirror finish with Struers® diamond polish (6µm, 3µm, and 1µm).

3.4.2 Optical and Electron Imaging

A 98% ethanol/2% nitric acid nital etchant was used to reveal the different microstructures on the polished surface. Optical imaging was done with Olympus® microscope and scanning electron imaging was carried out using a Zeiss® Leo 1530 field emission scanning electron microscopy. The SEM was equipped with a backscatter sensor and capable of electron dispersive spectrometry for element analysis.

3.4.3 Elemental Analysis

Elemental analysis of the sample was completed using energy-dispersive X-ray (EDX) and electron probe microanalyzer (EPMA). EDX test was completed with Oxford Instrument's AZtec EDX tool attached to the Zeiss Leo SEM. Point and line scan were performed with a scan time of 3 minutes; elemental mapping was completed with a scan time up to 20 min. EPMA was used to improve elemental mapping quality with higher precision. EPMA was completed using Dr. D.L Chen's SEM (model JEOL JXA8230 5-WDS) at Ryerson University.

3.4.4 Mechanical Testing

Hardness Measurement

Micrtohar5dness measurements were carried using a Clemex® Vickers hardness tester with an automatic stage control and measurement system to measure the micro-hardness. Indents were made

using a 300g force and 10 seconds indentation time. Hardness measurements were spaced with a clearance of at least 0.5 mm to avoid the work hardening effect from the previous indentations. A diagonal pattern with respect to the sample surface was used to capture all weld region as illustrated in Fig. 3.6.

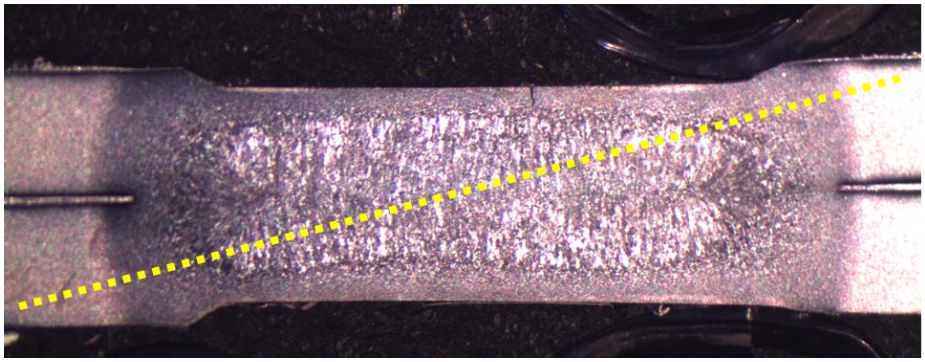

Figure 3.6 Hardness measurement pattern to capture hardness in FZ, HAZ, and BM

Lap Shear Test

The strength of the spot welds was measured using the tensile shear test. Samples were welded with an overlap of 40 mm and shimmed on both sides as shown in Fig. 3.7 to ensure axial tension. This overlap meets the minimum requirement suggested by Zhou et al [78]. Lap shear was pulled using an Instron model 4206 tensile tester at a pull rate of 5 mm/min.

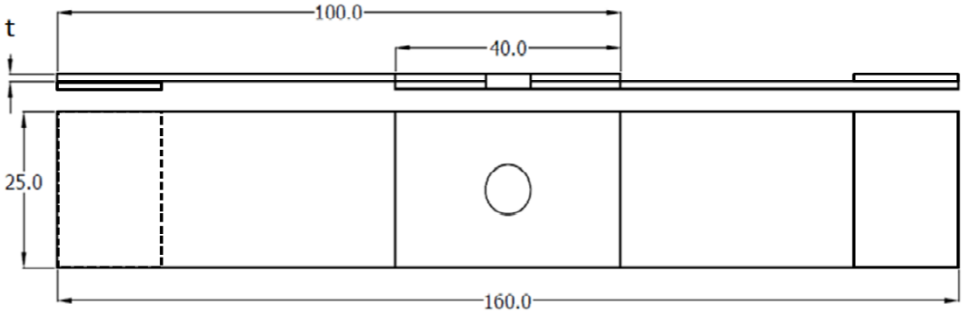

Figure 3.7 Lap-shear sample configuration

Chapter 4 Effects of Internal Oxides on Resistance Spot Welding

4.1 Overview of Internal Oxidation

The selective internal oxidation process was used to increase the wettability of the steel substrate to the zinc pool by providing a clean surface free from surface oxides. The presence and morphology of these internal oxides changed as different chemistries or annealing conditions were used. Variation

in the internal oxide condition leads to welding process instability because it affects the electric resistance profile of the sample. The objective of this chapter is to evaluate the effect of internal oxide introduced during the continuous annealing process on RSW of AHSS. First, the effect of internal oxidation will be compared to the as-received condition to verify the effect. Then, the welding response of materials produced using various annealing times will be compared to understand the effect of annealing on the resistance welding process. Results reported in this chapter helped to understand the effect of internal oxidation on the RSW process.

4.2 Effect of selective oxidation on the surface condition

Before testing the welding behavior, the difference between surface layer morphology of samples in the as-received and annealed conditions was characterized as the annealing process can affect properties such as the oxide layer condition and surface roughness, both of which impacts the resistance welding process. A comparison of those properties in the annealed and as-received condition is shown below.

Characterization of the oxide layer

Using the optical microscope, a layer of oxides was observed in samples in the annealed condition. However, the optical microscope's magnification and resolution cannot observe the detailed structure of this internal oxide layer. With the scanning electron imaging, higher magnification and better resolution allow observation of the oxides generated from the selective oxidation process (Fig 4.1a). Using the backscatter electron mode in SEM, the contrast between the oxides (MnO/SiO) and steel substrate was further enhanced due to the differences between their atomic weight, allowing easier identification of the oxides (Fig 4.1b). Two types of internal oxides, intragranular and intergranular, were observed in the sub-surface of the steel substrate in the annealed condition. The intragranular oxides were close to the surface of the steel and intergranular oxides grow along the grain boundaries. The intragranular oxides had a consistent thickness of 1.2μm, while the intergranular oxides were much longer and have more deviations. No presence of internal oxide was observed in samples of the as-received condition (Fig 4.1c).

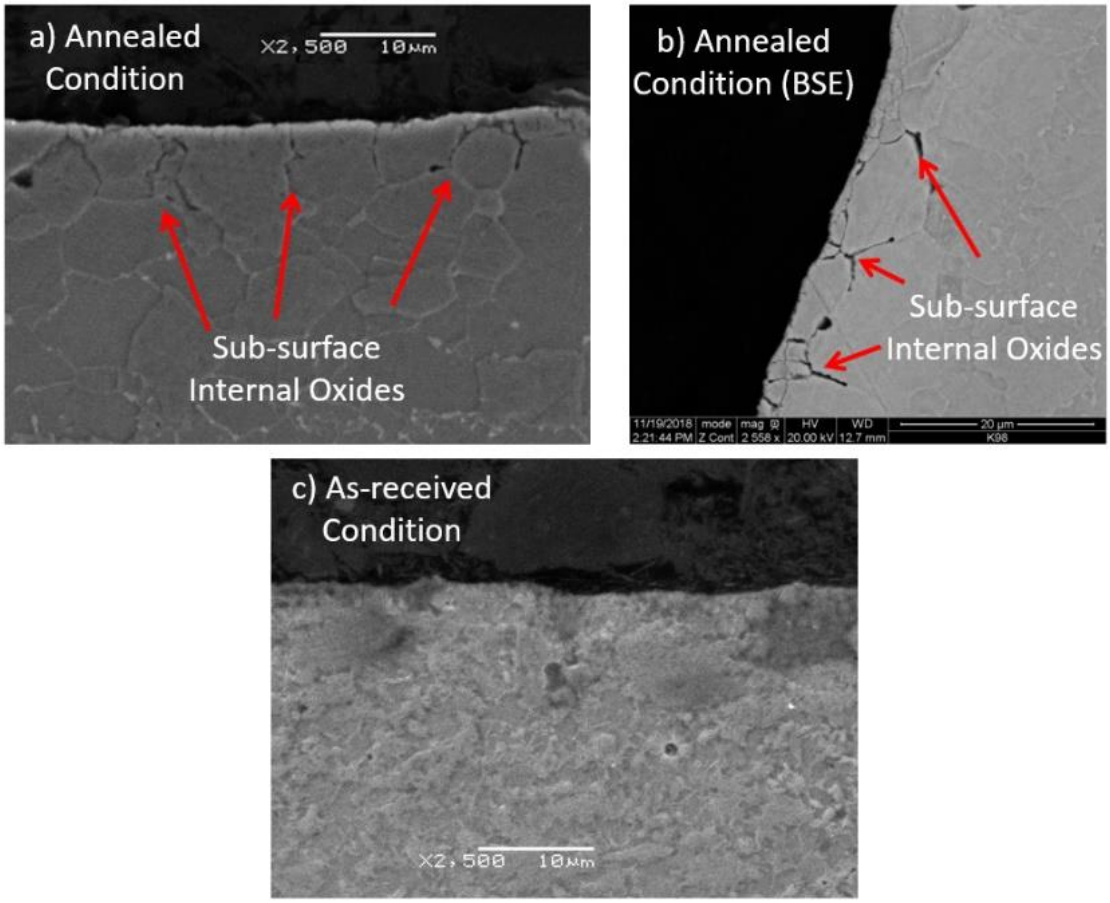

Figure 4.1 Surface and subsurface condition of CMnSi steel for a) annealed condition using secondary electron, b) annealed condition using back-scatter electron, and c) as-received condition using secondary electron.

Characterization of surface roughness

Surface morphology affected resistance spot welding as the surface contact area governs the contact resistance [41], [55]. Surface profilometry was used to map the roughness condition. From Fig. 4.2, a linear asperity pattern as a result of cold rolling was observed in both samples, where no observable visual difference can be observed in their asperity pattern. From the surface roughness data (Table 4.1), annealing reduces the arithmetical mean deviation (Ra) and root mean square (Rq) of the roughness by 10% and 8% respectively; the height difference (Rz and Rt) increase by 6% and 8% respectively. These measurements indicated that the surface of the annealed material is slightly smoother than the as-received surface.

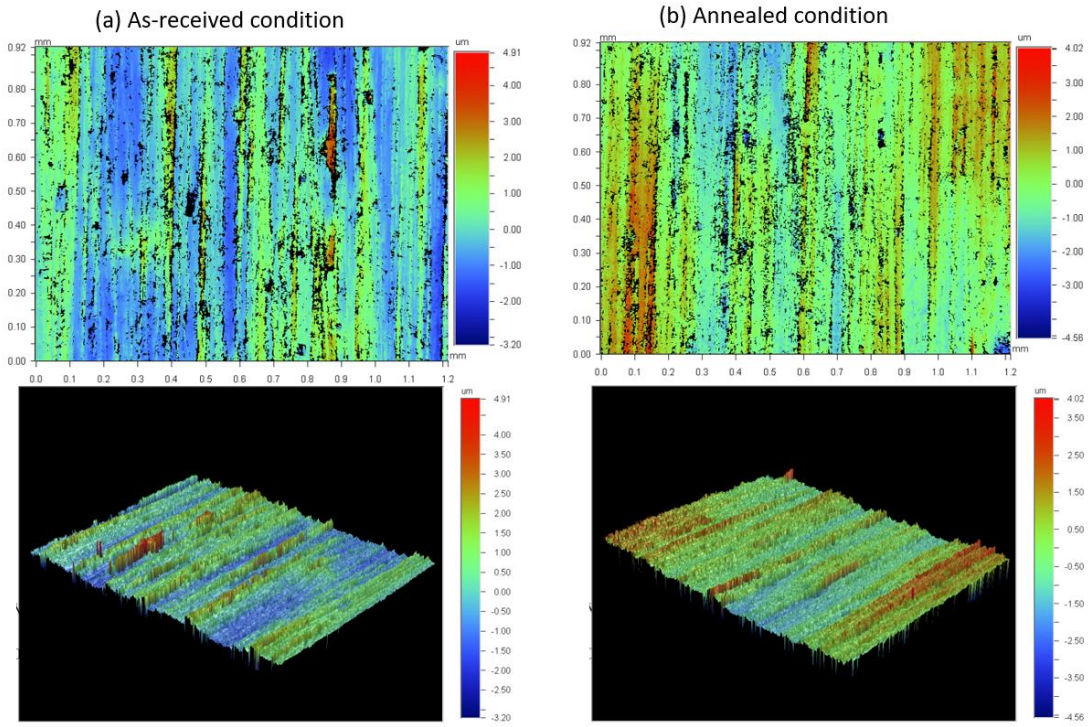

Figure 4.2 Surface profilometry of the (a) as-received and (b) annealed sample in 2D and 3D.

Table 4.1 Surface roughness measurement of the as-received and annealed samples

Condition	Ra (nm)	Rq (nm)	Rz (µm)	Rt (µm)
As-received	763	950	6.83	8.125
Annealed	688	878	7.22	8.765

Impact of Oxides and Surface Roughness on RSW

Both the oxide layer and surface roughness impact the resistance welding process as they change the surface contact resistance which determines the final heat generation. In the case of selective oxidation, the only difference observed between the as-received and the annealed condition was the presence of the internal oxides as the minimal difference in the surface roughness was observed between the annealed and as-received condition. Therefore, further works are required to evaluate the impact of internal oxides on the resistance welding process.

4.3 Effect of Internal Oxide on Welding Lobe

To measure the effect of internal oxide on RSW process, the welding lobe of as-received and annealed materials were measured and compared (Fig. 4.3). The weld lobe of the annealed condition shifted to the right, compared to weld lobe the as-received condition. No significant change in lobe width was observed. This shift in lobe curve indicates that welding annealed sample will require a change in welding parameters, but the weldability does not change, as the width of the lobe remains unaltered. Based on the change in weld lobe, the annealed condition requires a higher current to achieve a similar nugget as compared to the as-received condition. In other words, heat generation was decreased when internal oxides were introduced to the system. This phenomenon is counter-intuitive, as the introduction of oxides has been previously associated with increased contact resistance and heat input [52]. Therefore, the heat generation characteristic of internal oxides is different behavior compared to conventional surface oxides, which will be discussed in the following sections.

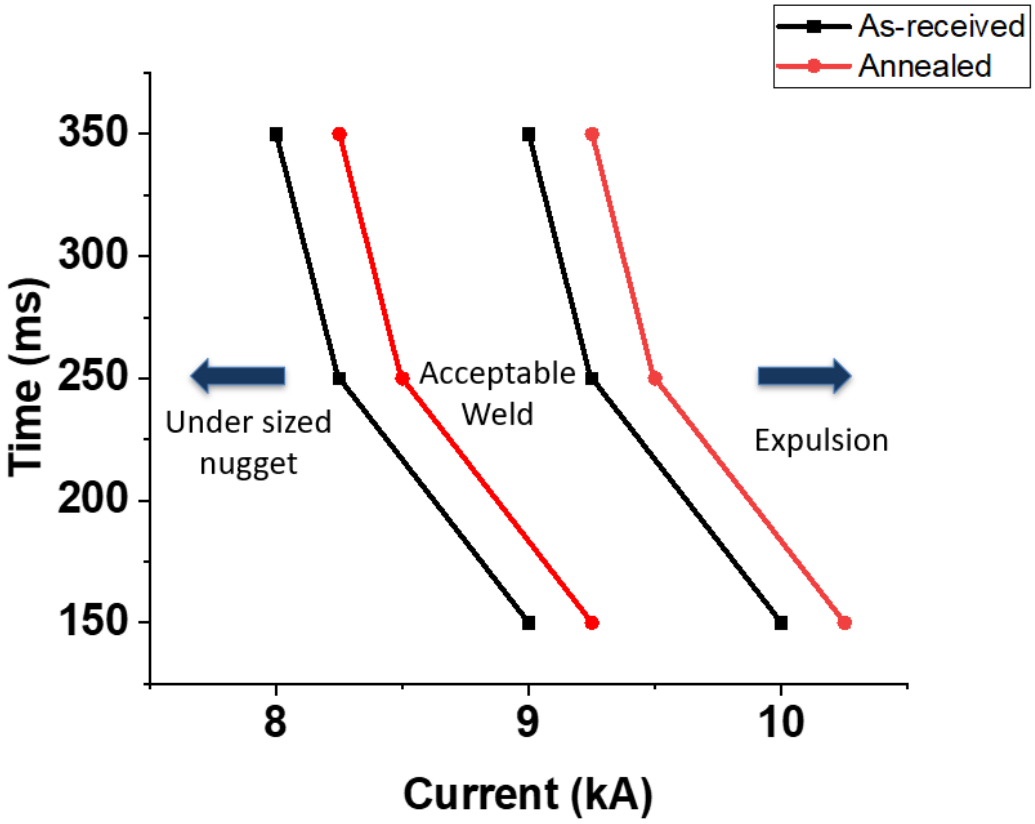

Figure 4.3 Weld lobe comparison between as-received (black) and annealed (red) sample.

4.4 Dynamic Resistance Analysis

To evaluate the decrease in heat input and change in weld lobe, dynamic resistance was measured for the CMnSi steel (Fig. 4.4a). The as-received condition (plotted in grey) has a typical dynamic response for uncoated steel as shown in the literature review.

A significant change in the dynamic resistance curve was observed in the annealed condition (Fig. 4.4a). The difference between the annealed and as-received condition was most pronounced in the interface dominated region of the weld cycle, where minimal melting has occurred, and the surface contact resistance dominates the resistance. Beyond welding time of 100 ms, resistance the difference between the two conditions diminished, as nugget development started to occur. The melting of the faying surface eliminated the presence of internal oxide. Therefore, the early stage of the welding process was of interest to investigate the effect of internal oxides on nugget development (Fig. 4.4b). This early-stage was further divided into different substages according to their representative characteristics.

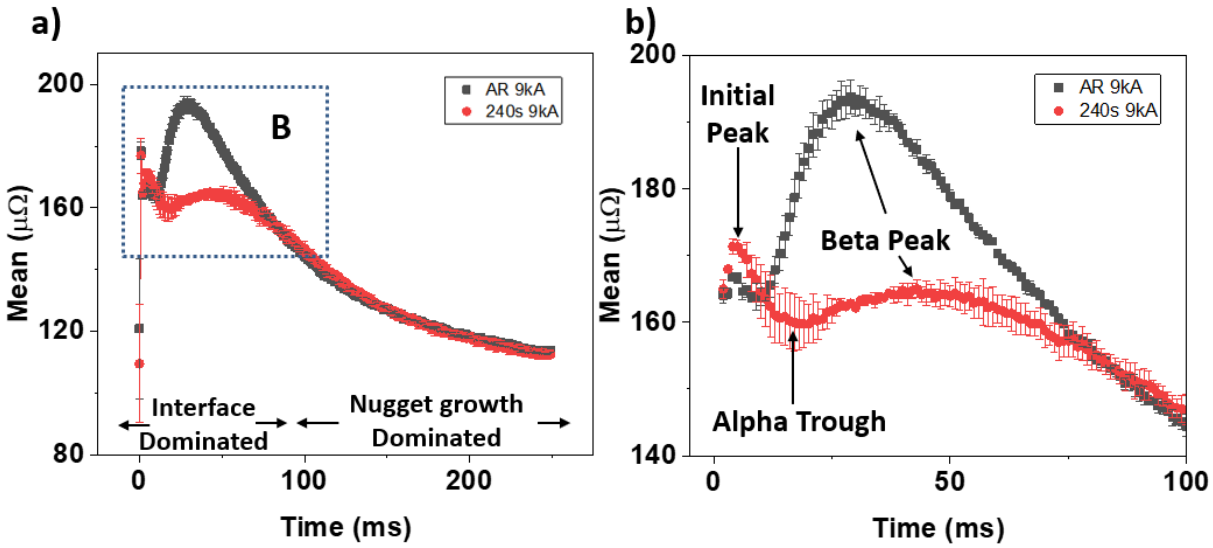

Figure 4.4 Dynamic resistance curve recorded (a) with emphasis on the weld beginning (b) shows the difference in beta peak and resistive behavior.

The initial dynamic electrical resistance can be treated as a quasi-static resistance measurement (Fig 4.4 b). The quasi-static resistance values are similar in both conditions, indicating a similar surface contact condition after the initial squeeze time despite the slight change in surface roughness observed with surface profilometry result in section 4.2. The annealed condition shows initial peak resistance about 10 μΩ higher that the as-received condition at the beginning of the welding process.

A comparison of the dynamic resistance of materials with and without surface oxide where it was reported that the sample with the surface oxide had static resistance that was 100 to 1000 μΩ [52]. In the case of surface oxides, the higher difference in resistance is created due to the rougher surface. As the internal oxide does not create additional surface asperity, the increase in dynamic resistance is mainly due to higher resistivity of the oxides.

The alpha trough occurs in the dynamic resistance immediately following the first resistance peak for both the annealed and as-received conditions. The resistance started to decrease to form the alpha trough due to the increase of the contact area at the faying surface as asperity softening further develops at a higher temperature. At the alpha trough, additional asperities softening is completed. The dynamic resistance starts to increase again as bulk heating is the only factor influencing the dynamic resistance. In the case of the annealed condition, the alpha trough is much wider and lower compared to the as-received condition. A difference in the dynamic resistance in the alpha trough region is not expected as a similar surface roughness was observed for both conditions, meaning no additional asperity in the annealed sample to be softened. This difference indicates there is a different phenomenon happening for the samples in the annealed condition.

As the weld cycle further progresses, the temperature at the faying surface reaches the melting temperature of the steel substrate. With the melting of the material at the faying surface, a liquid contact exists between the two samples, drastically reducing the contact resistance between the sheets. The dynamic resistance then starts to decrease with the reduction of contact resistance. This phenomenon was named the beta peak as it is often the highest resistance value during the weld cycle. Comparing the bulk heat region, the as-received condition has a steeper heating profile which resulted in a higher beta peak value. The annealed condition has a wider and lower beta peak. The bulk heating effect was suppressed by a different mechanism in this region, which causes a reduced electrical resistance and lower heat generation. Further investigations in surface development and heat input are necessary to understand the cause and impact of this change in dynamic behavior.

4.5 Analysis of Heat Input into the Welding Joint

The heat input was calculated using the Eqn. 3.1 with the measured instantaneous resistance and welding current (Fig. 4.5a). Although not all the heat generated contributed to weld nugget formation due to dissipation into the surrounding material, this calculated heat input value was a good comparison of the energy input into the weld growth between the two conditions. The total heat generated over the whole process was about 2700 J for both cases. By looking at the accumulated

difference in heat input (Fig. 4.5b), a clear energy input difference was observed. Most of the difference occurred at the beginning of the welding process in the interface dominated region, similar to the observed dynamic resistance. Despite the higher initial resistance in the annealed condition, welds in the annealed sample have lower heat input when compared to those in the as-received condition due to the less pronounced beta peak. As the welding cycle progresses into the nugget growth region, the difference in accumulated heat became more stable; the difference in heat generations becomes negligible later in the welding cycle. For a welding current of 8 kA, a difference of 80 J was measured. This was about 3% of the total heat energy input into the system. However, this fraction will be even larger if the heat loss in the process is discounted and only the heat responsible for nugget is accounted for the heat input calculation. Therefore, the annealed condition formed a smaller nugget according to the heat input analysis when using the same welding parameters.

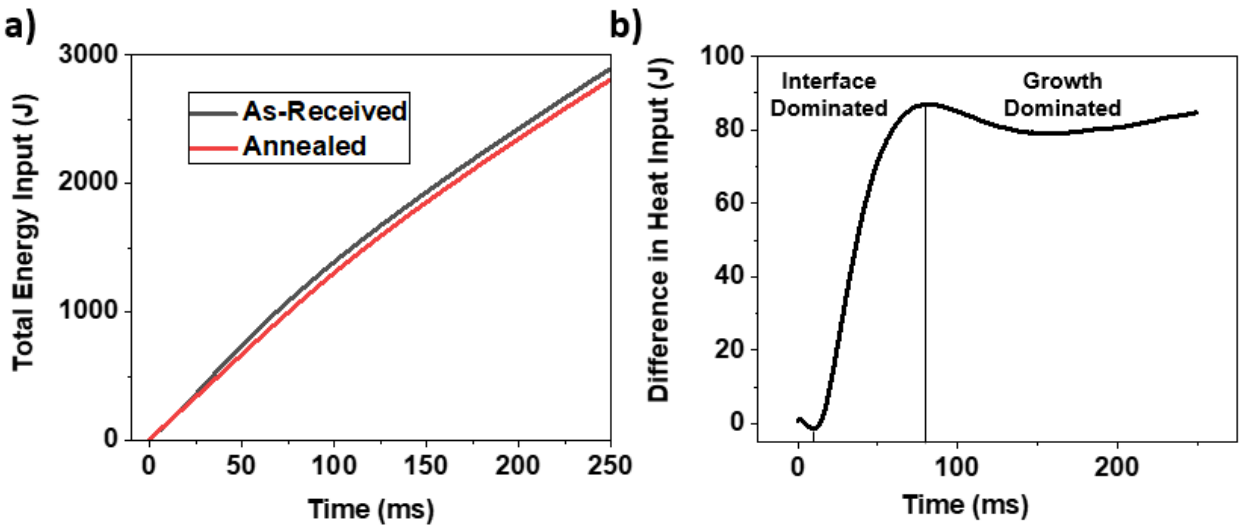

Figure 4.5 a) Heat input and b) comparison between as-received and annealed condition

4.6 Surface Development and its Impact on Dynamic Resistance

An interrupted test was used to monitor the different stages of surface development of the faying surface and match these surface developments to the measured dynamic resistance curve to gain insight into the difference in heat generation and nugget growth observed between the samples in the annealed and as-received conditions.

In the first stage of the welding process, softening of surface asperities is confirmed in both conditions (Fig. 4.6a&d). The annealed sample exhibited an earlier reduction in asperities compared to the as-received condition by 10 ms. This is a result of the higher contact resistivity due to the presence of the internal oxides at the sheet surface, which generated addition heat to promote faster softening of the asperities.

Following the asperity softening, the resistance increased in the as-received sample due to a higher material temperature from the build-up heat. The increase in dynamic resistance ends when melting occurs on the faying surface, which greatly reduces the contact resistance because the formation liquid contact surface eliminated the contact resistance (Fig. 4.6b). The phenomenon of bulk melting results in the formation of the beta peak in the dynamic resistance curve (Fig. 4.4b). In welds made on materials in the annealed condition, a ring of melting was first observed on the contact surface as the asperities soften (Fig. 4.6d). As the welding cycle progressed, the melted ring propagated throughout the faying surface. After 10 ms into the weld cycle, the resistance of samples in the annealed condition isa lower than the samples in the as-received condition as the contact resistance in the annealed condition was drastically reduced due to the presence of liquid contact between the two workpieces (Fig. 4.6e).

As welding time increased to beyond 40 ms, bulk metal melting can be observed in both samples. In samples in the annealed condition, the bulk melting happens within the surface melting region (Fig. 4.6f). For the annealed sample, the bulk melting also began later than in the as-received condition, which can be observed by comparing the size of bulk melting at 40 ms (Fig. 4.6c&f). As bulk melting begins, the heat generation in both the annealed and as-received conditions became identical as the internal oxides are dissolved and no longer plays a role. The dynamic resistance converges as the surface melting area are equal in both conditions.

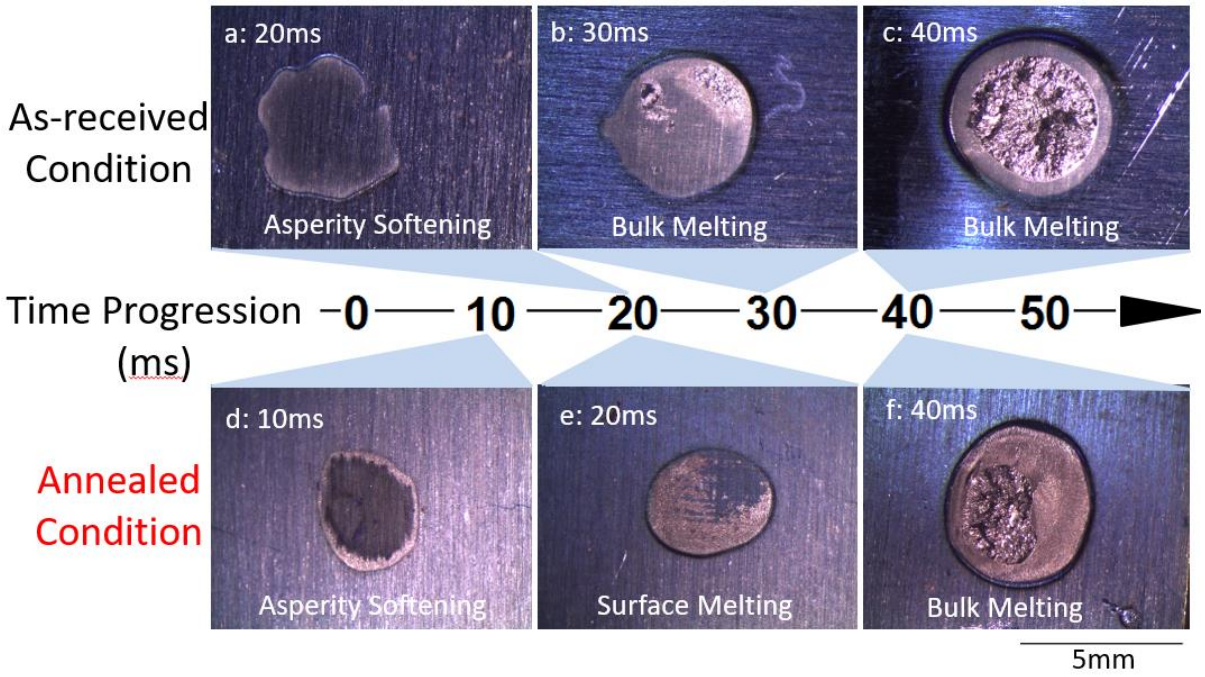

Figure 4.6 Surface development time-lapse observation from interrupted test

The presence of shallow surface melting was identified as the cause of changes in the timing of the welding process between the two conditions of CMnSi steels. The dynamic resistance curve confirmed that formation of surface melting reduces the resistance, creating a difference in the heat generation. This lack of heat input delays the formation of nugget in the annealed condition. A cross-sectional representation in Fig. 4.7 helps to understand the difference between the two mechanisms and how nugget was obtained. Samples in the annealed condition have an early surface melting mechanism which forms a liquid layer at the faying surface of the material. Presence of the liquid contact surface reduces the heat generation at the faying surface, delaying the bulk melting of the samples. As a result of reduced heat generation and delayed bulk melting, a smaller nugget is obtained in the samples in the annealed condition compared to the samples in the as-received condition.

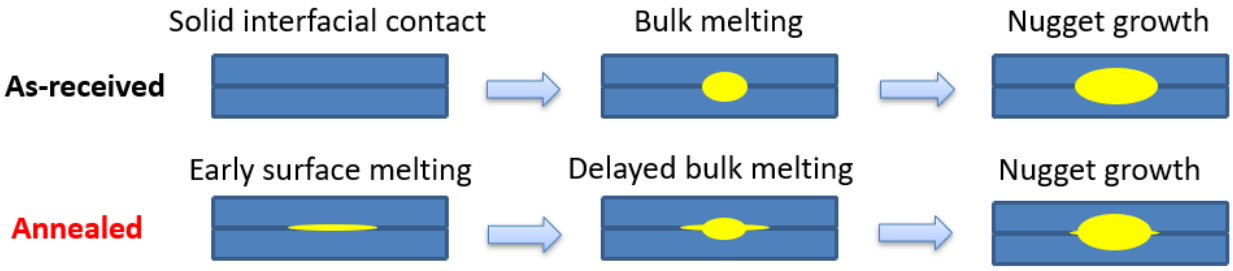

Figure 4.7 Schematic of the faying surface evolution illustrating different melting mechanisms between the as-received and annealed sample

4.7 Characterization of Localized Surface Melting

As mentioned in the previous section, shallow surface melting was observed in the interrupted test, which is determined to be a result of the internal oxidation. Cross-sections of welded joints made during the interrupted tests were observed to confirm this phenomenon. The first 10 ms of the weld cycle corresponds to the asperity softening period, where asperities are crushed by the electrode pressure resulting in a continuous contact between the two sample surfaces. When welding in the annealed condition, the faying surface and the internal oxide layer can be clearly identified after the first 10 ms of the welding process (Fig. 4.8a). In this stage, the overall morphology of the oxides remains similar to the as-annealed condition. As welding proceeds beyond 20 ms, evidence of surface melting may be seen, but the liquid does not fully cover the faying surface. In the area where the surface is free of liquid, the faying surface is still visible, and its structure resembles what was observed in the 10 ms case (Fig. 4.8b). However, in this stage of the welding cycle, oxide coarsening has started due to the temperature increase in this area (Fig. 4.8b). In the other areas where surface melting has occurred, a localized melting and solidification were observed, effectively eliminating the faying surface (Fig. 4.8c). While the faying can no longer be observed where the surface melting has occurred, intergranular oxides were not eliminated. The presence of the oxides indicated that the melting only occurred near the surface area. This observation confirmed the presence of a thin liquid layer during the earlier stage in the annealed condition observed in the previous sections. As welding time increased to 40 ms, bulk melting occurred (Fig. 4.8d). Bulk melting can be identified by the uniform microstructure and lack of oxides, as they are dissolved in the molten nugget. In contrast to the surface evolution in the annealed material, surface localized melting is not observed in the as-received condition (Fig. 4.9a&b). The faying surface remained visible until the bulk melting occurs by comparing the microstructural images of surface evolution in both cases (Fig. 4.8 & 4.9), the

mechanism of localized surface melting in the annealed condition is confirmed to be the cause of change in heat generation in the early stage of the welding cycle.

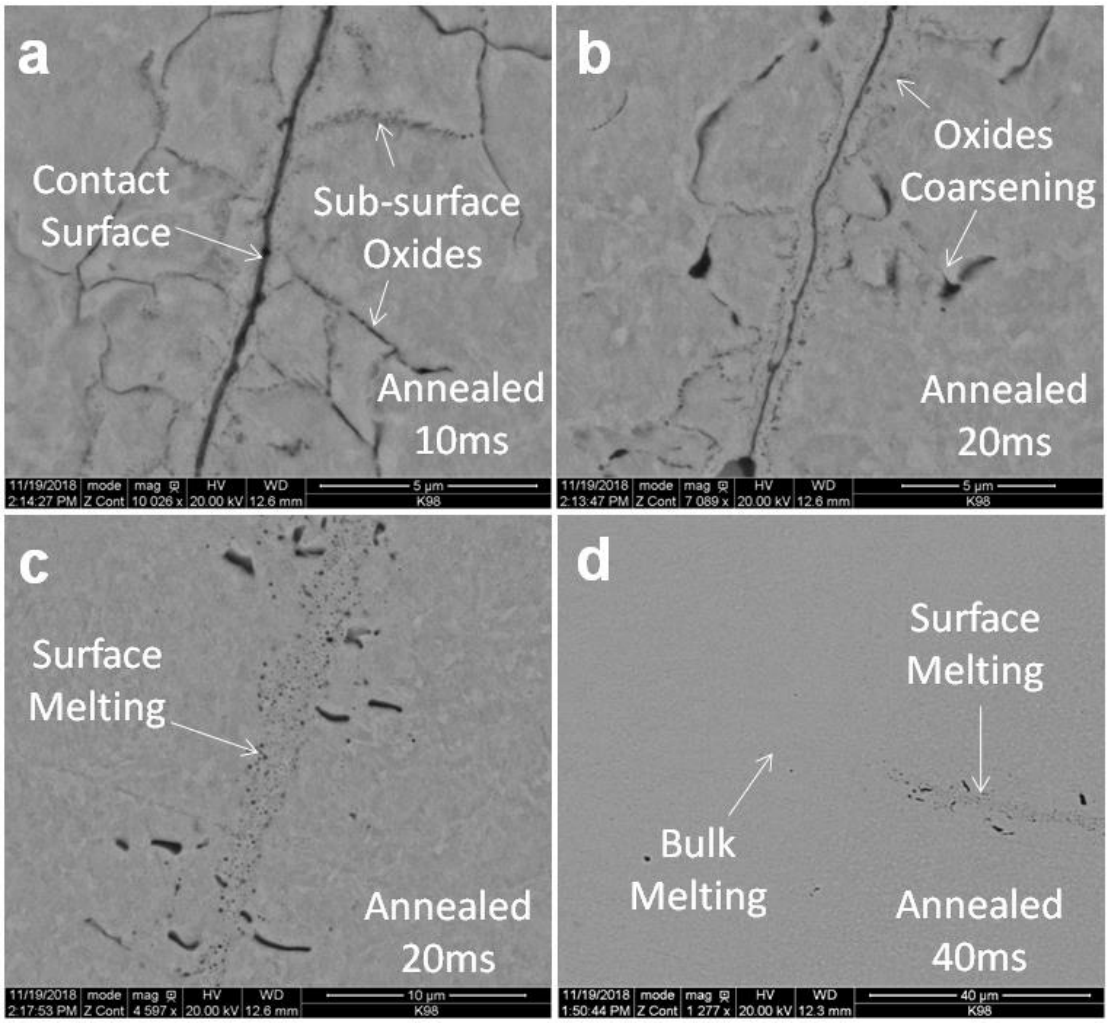

Figure 4.8 Change in the faying surface of the annealed condition during the first portion of the welding cycle featuring a) solid contact surface featuring sub-surface oxide at 10 ms weld time; b) after heating for 20 ms, the contact surface is visible in areas without surface melting; c) in areas where surface melting occurred, a resolidified molten layer is observed; d) the bulk melting was observed at 40 ms where oxides are mixed into the steel, resulting in a uniform structure.

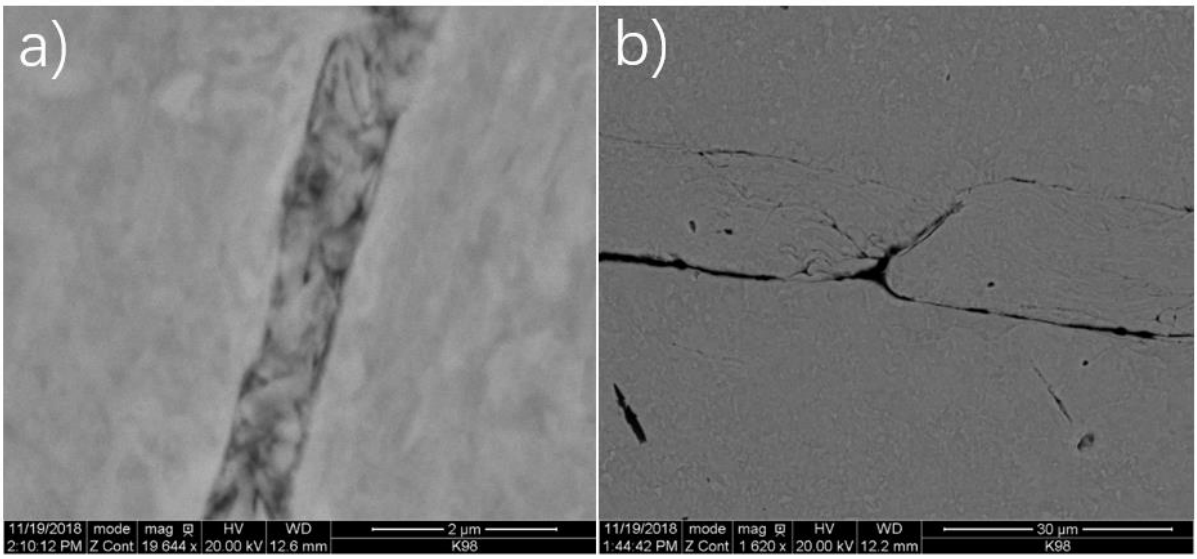

Figure 4.9 Cross-section of samples welded in the as-received condition showing a visible contact surface without formation of surface melting at a) 10 ms and b) 30 ms

4.8 Variations in Internal Oxide Condition on RSW Process

As the effect of internal oxide presence on the welding development has been identified, it is important to understand how variations in the internal oxide conditions, such as thickness and composition of the internal oxide layer, can affect the welding process. This section will discuss the effect of prolonged annealing time and variation in steel chemistry on RSW of selectively internal oxidized CMnSi steels.

4.8.1 Effect of Prolonged Annealing Time

To evaluate the effect of prolonged annealing time, when annealing time during processing increases, diffusion of oxygen into the steel surface increases, forming a thicker internal oxide layer. However, even with a thicker oxides layer, the dynamic resistance measurements taken during the welding cycle show that the dynamic curves from both annealing conditions overlap with each other (Fig 4.10a). Statistical analysis such as t-test was used to confirm the two curves to be not distinguishable for the CMnSi 2/0.7 grade steel. A similar result was obtained for the CMnSi 2/1.7 grade steel (Fig 4.10b). This result shows that additional annealing beyond 240 s has no observable effects on the resistance welding schedule of the steel.

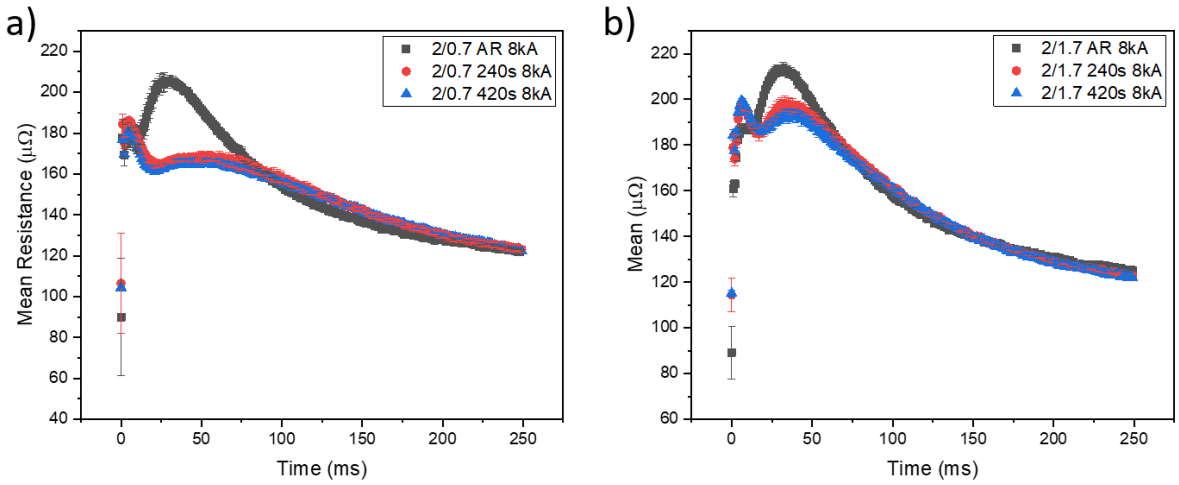

Figure 4.10 Comparison of dynamic resistance between difference annealing time for both a) CMnSi 2/0.7 and b) CMnSi 2/1.7.

4.8.2 Effect of Variation in Steel Chemistry

The properties of internal oxide are affected by steel chemistry. Higher alloying contents increase the amount of oxide formation. In addition to changing the internal oxide formation, additional alloying elements influence the bulk resistance. This leads to a difference in the as-received condition (Fig 4.11a). To normalize the change in bulk resistance, the difference between the as-received condition and the annealed condition was used to compare between the two steel chemistries (Fig. 4.11b). With increased alloying component in the CMnSi 2/1.7 grade steel, a lower reduction of dynamic resistance is observed. The time at which the difference peaked is similar for both chemistries, showing that change in oxide condition does not affect surface melting. As the surface melting effect is already triggered at lower oxide level, additional oxide from changing steel only increases the electrical resistance.

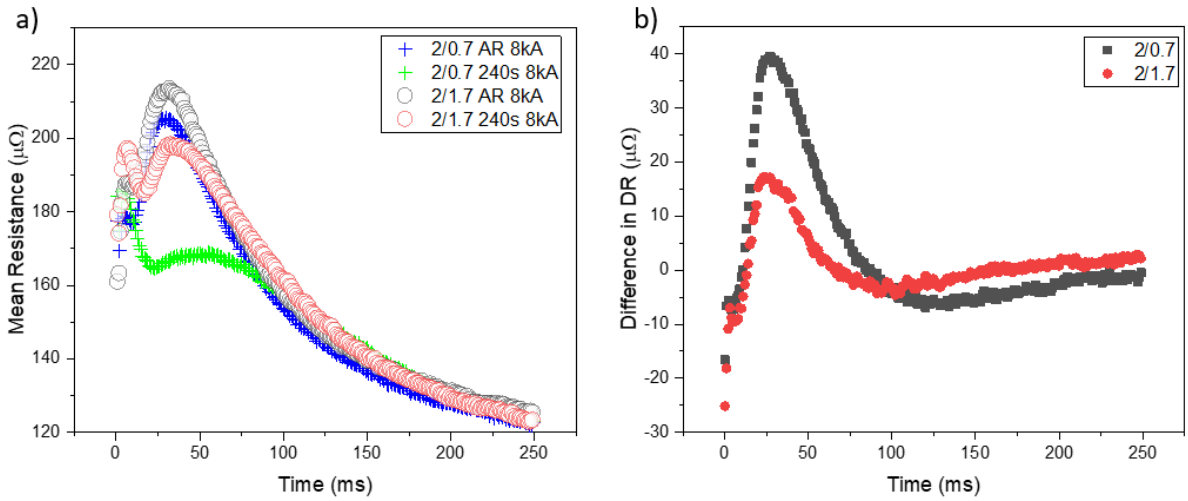

Figure 4.11 a) Dynamic resistance in as-received and annealed conditions and b) the change in dynamic resistance due to annealing.

4.9 Summary

Presence of these oxide layers was shown to affect the resistance welding process. Earlier melting of the surface was observed from the interrupted samples. Liquid layer from the surface melting reduced the contact resistance in the faying surface, in turn reduced the heat input into the weld. With annealing, smaller nuggets were obtained using the same welding parameter. Materials treated with different annealing time were shown to not impact the surface melting mechanism while increasing the alloying content in steel chemistry was shown to increase electrical resistance while not affecting the surface melting mechanism. There should be a limit on the minimum annealing time where further reducing the annealing time will stop the formation of surface melting mechanism; however, such value was not found in this study.

Chapter 5 Effect of Variation in Zn Diffusion Layer in Press-hardening Steel on its RSW Process

5.1 Overview

Press-hardening steel (PHS) requires a thermal process to achieve its high strength. With elevated temperature during the heat treatment, Zn from the GA coating diffuses into the steel substrate forming a diffusion layer. This diffusion process is dependent on the heat-treatment condition of the press-hardening process. Variations in the diffusion layer condition affect the electrical resistivity and affect the RSW process. In this chapter, various diffusion conditions were created through changes in the press-hardening parameters and initial coating weight to observe the effect of diffusion layer composition and thickness on resistance spot welding.

5.2 Characterization of the GA coating layer and the Zn diffusion layer

To characterize the effect of heat-treatment on the diffusion layer, the diffusion layer conditions were characterized in the as-received and post heat-treated conditions. In the as-received condition, the base material had a pearlitic/ferritic microstructure was observed (Fig. 5.1a). A GA coating was present in the as-received condition of the PHS (Fig. 5.1b&c). The GA layer mainly comprised of a δ phase Zn with a Γ phase Al-Zn-Fe interlayer between the GA and the steel substrate, as the result of phase transformations during the galvanizing process (Fig. 5.1d).

After the heat treatment, Zn from the original GA coating layer diffused into the steel substrate to form a zinc diffusion layer comprised of a uniform α-Fe (Zn) solid-solution structure as shown in the EPMA map (Fig. 5.2). This structure differed significantly from the as-received GA coating with missing gamma and delta phases. No trace of Al remained in the heat-treated condition. Zinc oxide formation on the surface was observed and removed using sandblasting, therefore not present in the EPMA scan.

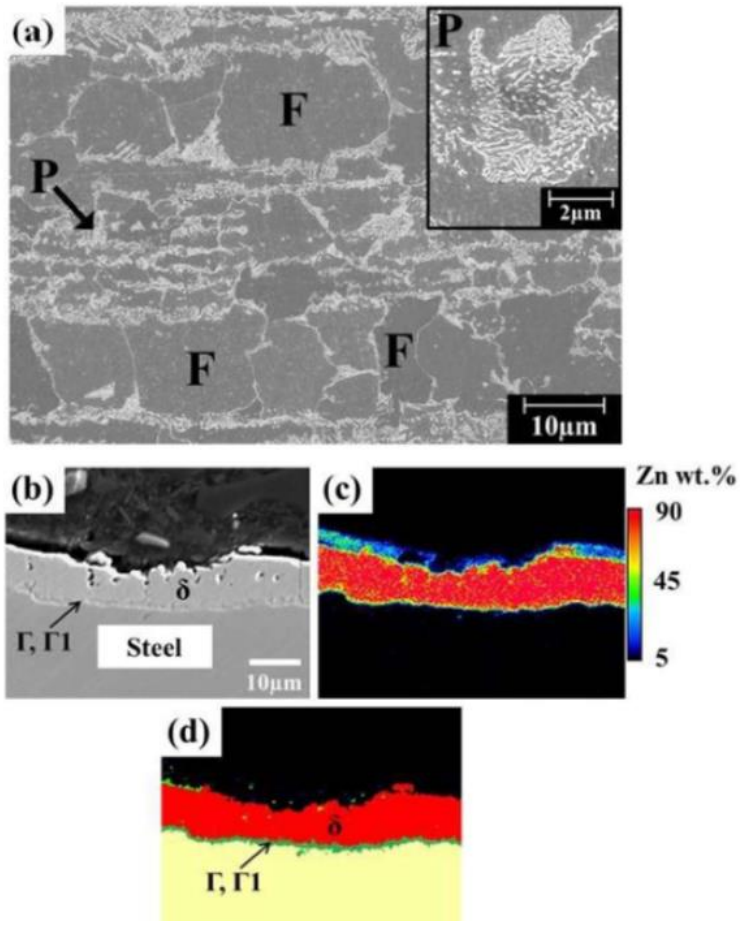

Figure 5.1 As-received condition of the press-hardening: a) Representative microstructure of the as-received material, cross-sectional, b) SEM micrograph, c) EPMA Zn distribution map, d) phase map [76]

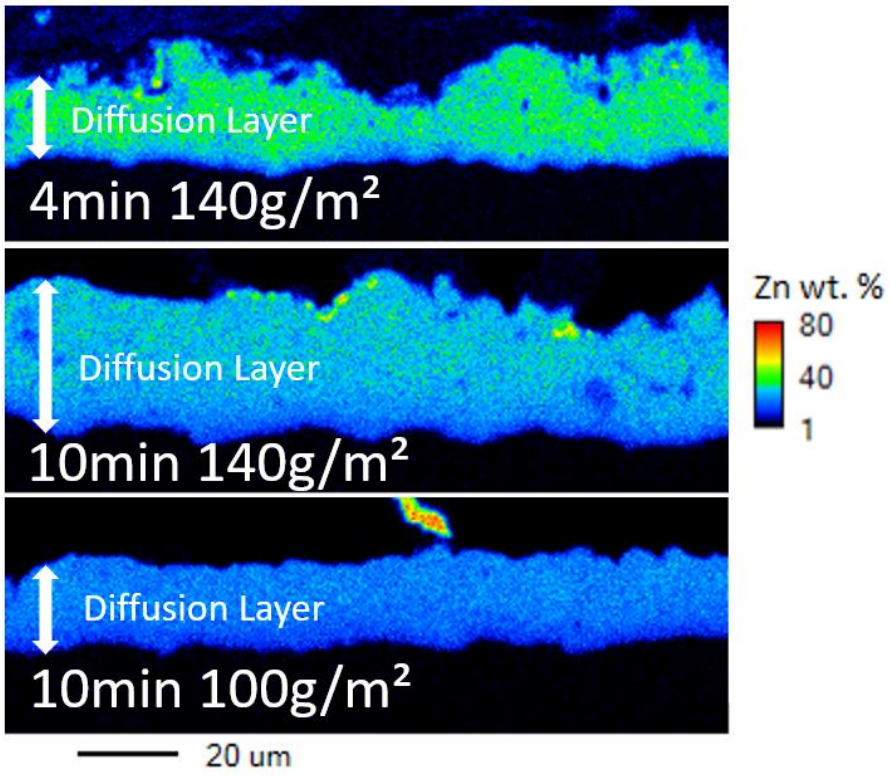

Figure 5.2 EPMA mapping showing the concentration of Zn in the diffusion layer after heat treatments with different coating weights: a) 4min @140g/m², b) 10min @140g/m², and c) 10min @100g/m².

5.3 Effect of heat-treatment parameters on diffusion layer condition

The Zn diffusion layer thickness and Zn concentration were correlated to the heat-treatment time and the initial GA coating weight (Fig. 5.3). With increasing heat-treatment time, a thicker diffusion layer was formed as Zn had additional time to diffuse with the steel substrate (Fig. 5.3a). Consequently, the Zn concentration decreased as the available Zn from the GA layer was distributed over a larger volume as the diffusion layer grew (Fig 5.3b).

Effect of Heat-treatment time

The change in both the diffusion layer thickness and composition were not linear with respect to the heat treatment time. As the heat-treatment time increased at a shorter treatment time (from 4 min to 7 min), a larger difference in coating thickness and Zn composition was observed compared to similar change at a higher heat-treatment time (from 7 min to 10 min). This phenomenon was explained by Fick's second law of diffusion, where diffusion distance increases as a function of the square root of time [77]. Therefore, the Zn diffusion growth rate decreases later in the heat-treatment period as the concentration gradient decreases. In addition, the formation of Zn oxide on the surface also consumed Zn from the GA layer. Formation of oxide contributed to the depletion of Zn from GA, further reducing the concentration gradient.

Effect of Initial Coating Weight

A similar trend in change of diffusion layer thickness was observed when materials with different coating thicknesses were heat-treated. By increasing the GA coating thickness, additional Zn is available for diffusion, resulting in a thicker diffusion layer and higher Zn concentration in the diffusion layer as well (Fig 5.3).

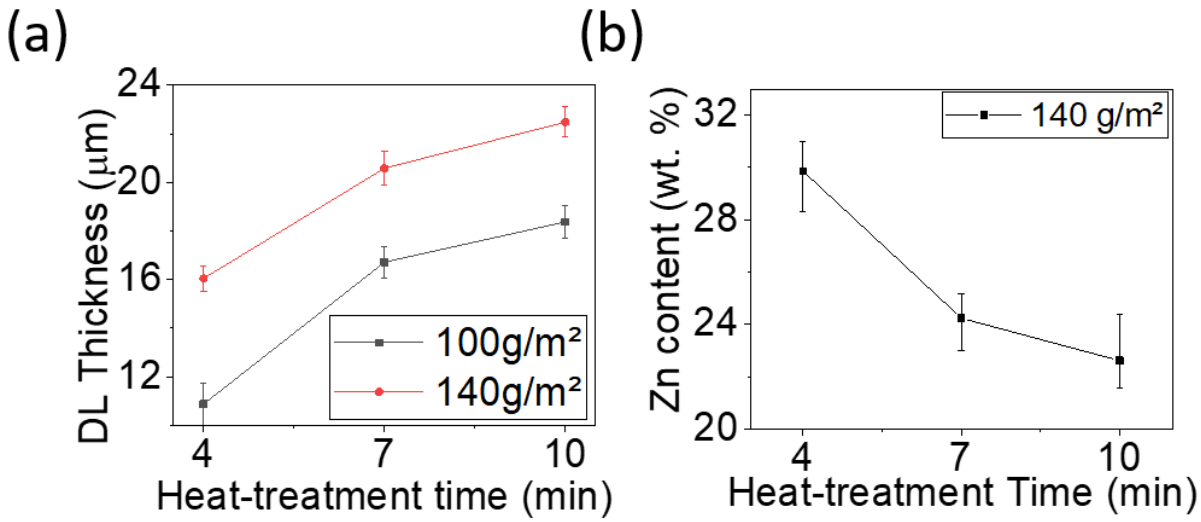

Figure 5.3 a) the diffusion layer thickness and b) the zinc content (wt%) at different heat-treatment times.

5.4 Surface Development and Correlation to Dynamic resistance

As the diffusion layer will have a different resistivity compared to the substrate, which will affect the heat generation during the resistance welding process. Therefore, the dynamic resistance curve needs to be measured to understand how the diffusion layer affects the welding process. The dynamic resistance curve was recorded to study the change between different heat-treatment conditions. As the dynamic resistance curve is different from the coated or uncoated dynamic resistance curve reported in the literature, an interrupted test is used to correlate the dynamic resistance in the earlier welding stage with the weld sample surface evolution (Fig. 5.4).

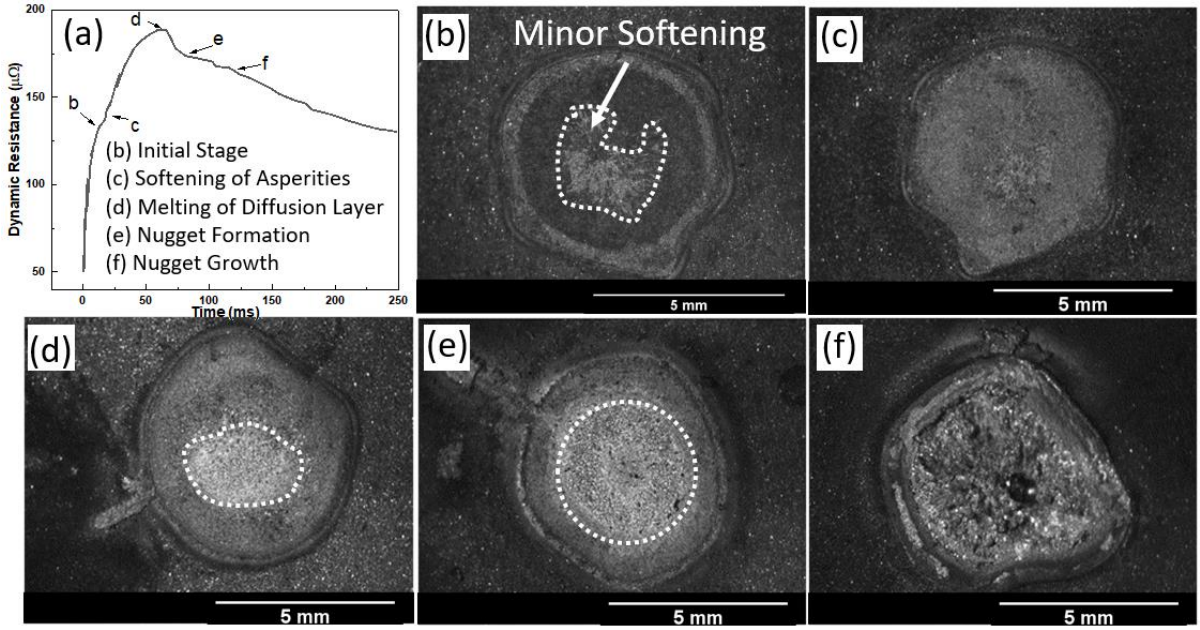

Figure 5.4 a) Dynamic resistance curve and its correlation to the surface development featuring: b) initial stage, c) asperity softening, d) melting of the diffusion layer, e) nugget formation, and f) nugget growth.

5.5 Comparison of the dynamic resistance between diffusion conditions

With an understanding of the correlation between dynamic resistance and surface condition, the dynamic resistance curve can be used to compare the difference between the welding behavior in the different heat-treatment conditions as shown in Fig. 5.5. A higher initial and peak resistances are observed in samples with a longer heat-treatment time (Fig. 5.5b). A higher resistance indicates that there will be additional heat-generation due to Joule heating, which accelerates the melting at the contact surface. As shown in Fig. 5.4, the nugget formation starts right after the peak resistance is reached. Therefore, the earlier peak resistance observed with a longer heat treatment time indicates an earlier nugget formation. It is worth noting that a similar peak resistance was measured for the heat-treatment time of 7 min and 10 min (Fig. 5.5b). This similarity came from the minimal difference in the diffusion layer thickness and Zn-Fe composition between the two heat-treatment times (Fig. 5.3).

Once nugget growth starts, the dynamic resistance between different diffusion layer conditions became similar because the diffusion layer is consumed by the nugget, so after nugget growth begins, the diffusion layer no longer contributes to resistivity increase.

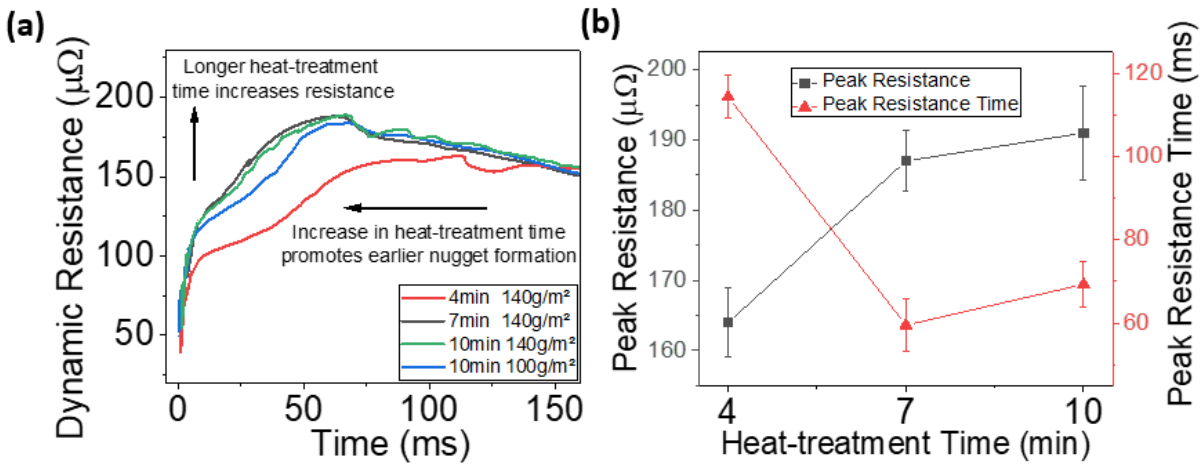

Figure 5.5 a) Dynamic resistance curve measure with different heat treatment conditions and b) the peak resistance time and value for different heat-treatment conditions.

5.6 Process window and lobe curve

To study the effect of heat-treatment on the RSW process, the weld lobe of materials subjected to various heat-treatment times were compared (Fig. 5.6). Recalling from section 2.3.5, the weld lobe is defined by the minimum nugget size and the expulsion condition. To calculate the minimum required nugget size for PHS, a c-value of 4.5 is used as opposed to 4.0 suggested by the AWS D8.9 standard to better reflect the high strength of the material.

Both the weld lobe curve width and location are affected by the material in the heat-treatment schedule (diffusion layer thickness and composition) as shown in Fig. 5.6. It was observed that the materials heat-treated for longer times had weld lobes that were located to the left of the materials heat-treated for a shorter time. When the weld lobe is further left, it indicates that less current is required to

achieve the same minimum nugget size. Similarly, this increase in resistance lowers the expulsion current limit. This observation agrees with the dynamic resistance results, which showed that longer heat-treated samples have higher resistance and reaches their peak resistance earlier in the weld cycle (Fig. 5.5b). The effect of heat-treatment on the lobe curve shift is less severe at longer welding time. As heat generation from contact resistance is greatly reduced after the nugget growth starts, longer welding time reduces the impact of surface conditions as the proportion of heat generated from bulk heating increases. The width of the weld lobe also increases by 0.5 kA when heat-treatment is increased from 4 min to 10 min, however, it should be noted that all the conditions have a lobe width above 2 kA at the suggested total welding time of 500 ms (Fig. 5.6). To take into consideration how changes in diffusion layer thickness and composition affect weldability, a combined lobe with the extreme conditions (highest minimum nugget and lowest expulsion limits) was constructed. From the combined lobe, an effective operating window above 1.5 kA was observed at a 500 ms welding time when heat-treating time is not controlled. This lobe width exceeds the typical weld lobe width of 1 kA used by the automotive industry to indicate sufficient welding robustness for manufacturing.

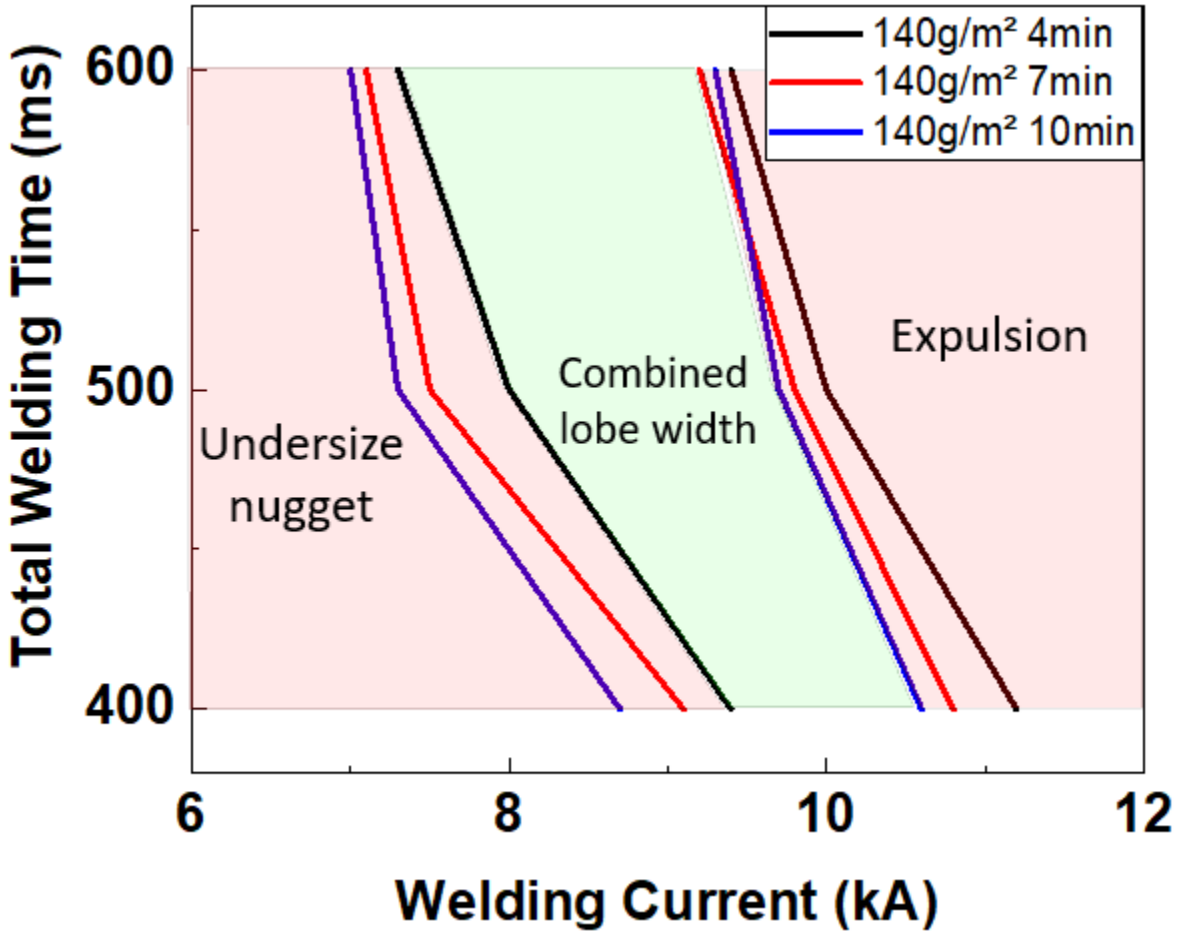

Figure 5.6 Weld lobe curve at different heat treatment conditions showing the shift in lobe curve as heat treatment condition changes.

5.7 Mechanical properties and fracture mode

As the heat-treatment was shown to affect the nugget formation in RSW, it is important to investigate in its impact on mechanical strength. A representative load-displacement curve is shown in Fig. 5.7a; furthermore, all samples failed in button pull-out mode (Fig. 5.8a). When welded using the same welding parameters, no difference in the maximum load was observed, despite the difference in nugget size (Fig. 5.7b). To investigate this mechanical loading behavior, a fracture surface analysis of tensile testing was performed. It was found that fracture initiated in the heat-affected zone (HAZ) and

outside of the nugget area (Fig. 5.8a). The fracture surface was further characterized using SEM (Fig. 5.8b). A closer inspection of the crack initiation area (Fig. 5.8c) revealed that fracture occurred in a ductile fashion. As the crack propagated during the loading, the failure mode became increasingly brittle with signs of cleavage cracking (Fig. 5.8d). This initial ductile fracture indicates that the microstructural changes in the HAZ are indeed the fracture initiation point. Further analysis of the HAZ can help understanding why increasing nugget size did not increase the joint strength.

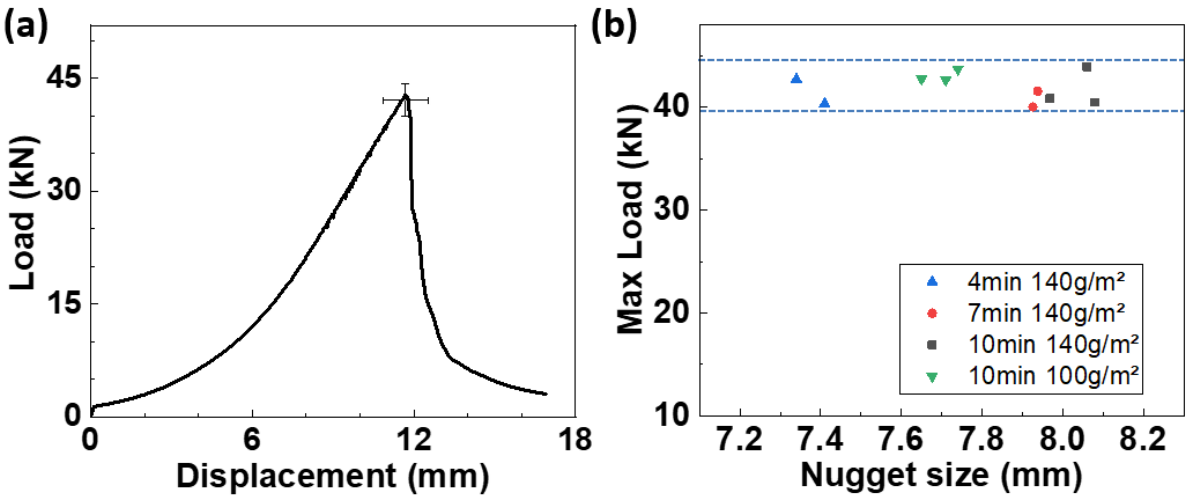

Figure 5.7 Lap shear results showing a) a typical displacement-load curve and b) distribution of maximum tensile load in different heat-treatment condition and their measured peak resistance.

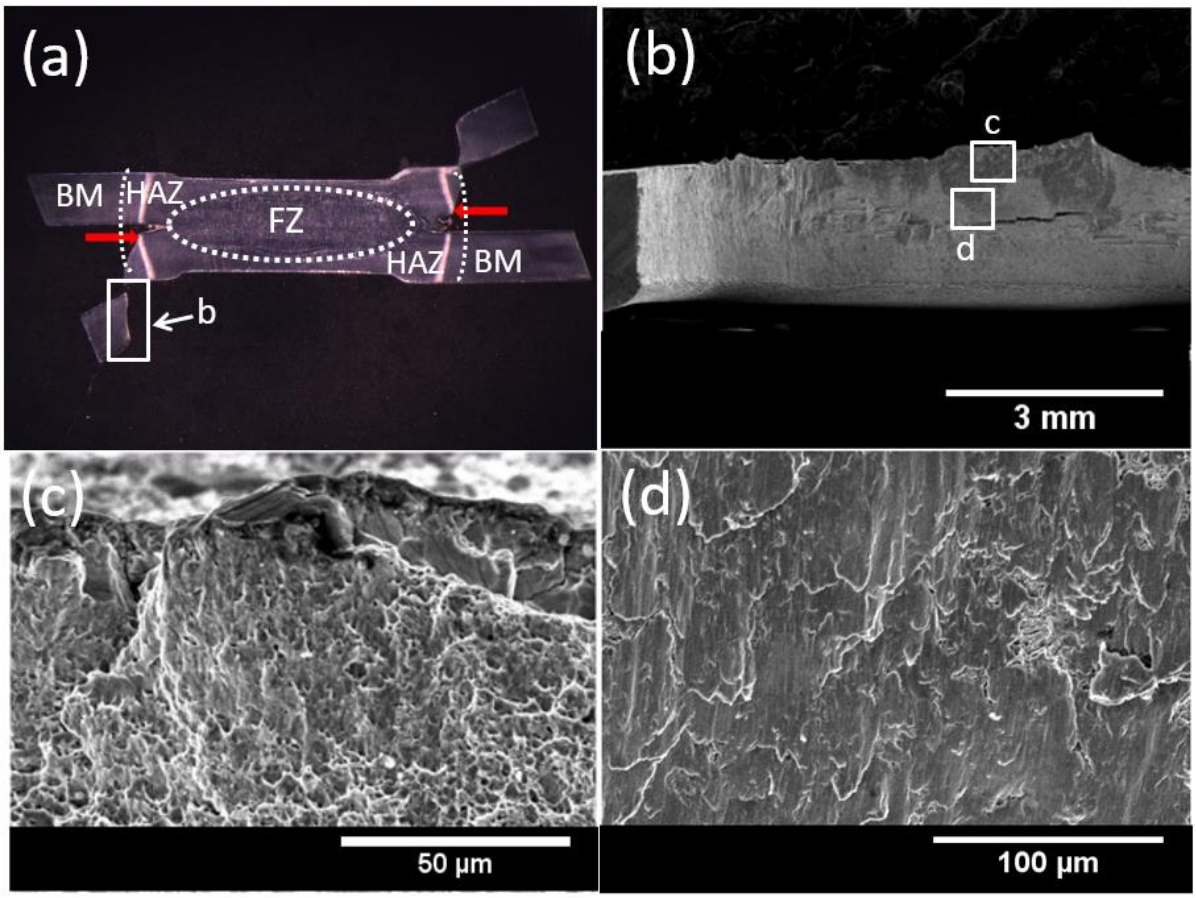

Figure 5.8 Cross-sectional imaging of a) nugget pullout failure observed in PHS lap shear testing, b) macroscopic picture of the fracture surface around the nugget pull out, c) ductile failure mode near the crack initiation points, and d) brittle cleavage failure mode as the crack propagates.

5.8 Hardness measurement

The hardness profiles across the welds were measured to understand how heat-treatment conditions affect the HAZ when welded with consistent parameters (Fig. 5.9a). The fusion zone (FZ) and base metal (BM) both have high hardness due to their martensitic structure. However, significant softening was observed over the HAZ which is associated with the martensite tempering that consequently affected the strength of the joint. Fig. 5.9b showed that with an increase in the heat-

treatment time, both the width of the HAZ, and the degree of softening increased, resulting in a higher loss in the mechanical strength at a longer heat-treatment time. However, a higher resistance at the long heat-treatment time also created a larger nugget which increases the joint strength. The effect of increasing nugget size is compensated by the decrease in HAZ strength, explaining why similar tensile shear strength values were obtained from the different heat-treatment conditions (Fig. 5.9b).

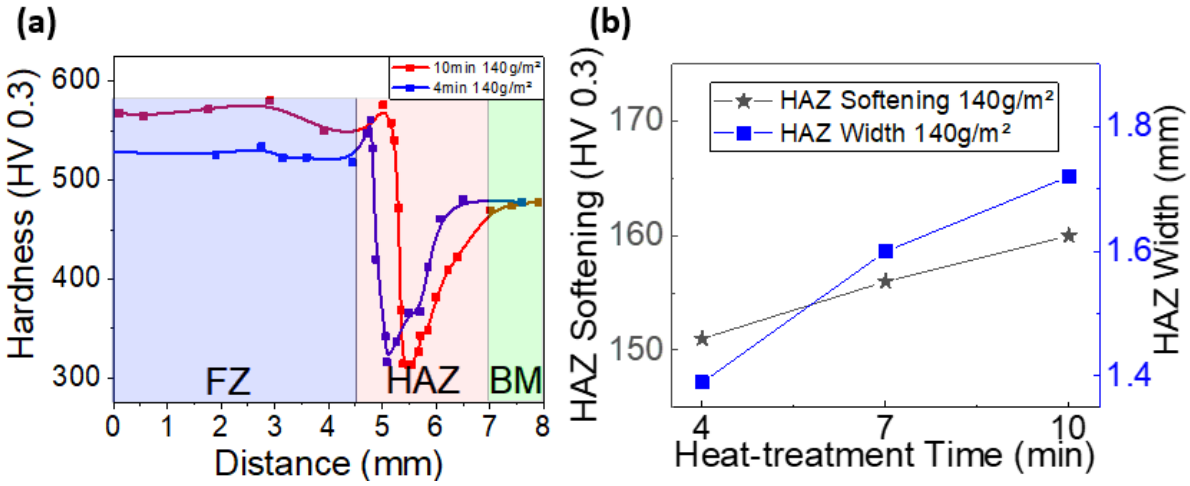

Figure 5.9 Hardness mapping showing the heat-affected zone hardness drop

5.9 Summary

A change in heat-treatment condition alters the diffusion layer on Zn coated PHS based on SEM and EPMA results, and the diffusion layer condition affects the electrical resistance behavior during welding. Lobe curve width is above 2 kA for each individual condition, and a combined lobe width above 1.5 kA is observed. With increased heat treatment time, the weld lobe shifted to the left due to the material's higher resistance. The left shifting lobe at the longer heat-treatment time indicates that larger nugget will form when welded using the same welding parameter. The mechanical test shows that no significant difference in lap-shear results exists between the materials welded that had different heat-treating conditions. More severe martensite tempering was observed in samples with

longer treatment time, neutralizing the effect of increasing nugget size. Therefore, the RSW process can ensure a sound weld in PHS joint under a variation of heat-treatment of PHS material.

Chapter 6 Heat Input Analysis of Dynamic Resistance for Monitoring and Controlling the RSW Process

6.1 Overview

In chapter 4 and 5, internal oxidation and Zn coating diffusion were shown to affect the resistance spot welding process and influence the nugget formation by changing the surface resistance profile. To ensure the consistency in the weld performance, weld quality controls were necessary. Multiple testing methods, such as ultrasonic testing, chisel testing, or peel testing, were developed to measure the weld size. However, these quality control methods are impractical for the manufacturing environment due to their high cost, long cycle time, or damage to the parts. Compared to these testing methods, dynamic resistance measurement emerges as a suitable candidate for weld monitoring, because most existing welding machines have the capability of extracting electrical data without the need for additional equipment. In this chapter, dynamic resistance analysis is used to monitor variation in weld size due to surface conditions and to correct potential undersized weld.

6.2 Heat Input Analysis of Resistance Features

When analyzing the electrical dynamic resistance, different statistical analysis of the dynamic resistance curve, such as the initial resistance, peak resistance, resistance drop, up-slope, and downslope (Fig. 6.1) have been used to monitor the weld development. Recent findings by Choi et al. have shown that most of the individual resistive analysis, such as only considering the peak resistance, poorly reflect the overall weld quality [53]. The method of computing heat input can incorporate the different resistance statistics into a single comprehensive value. Given the Joule heating formula shown in chapter 3 (Eqn. 3.1), the heat input is proportional to the area under the resistance curve assuming a constant welding current was used (Fig. 6.2). Thus, the heat input analysis has taken into account the dynamic resistance over the entire welding cycle, which

theoretically will provide a better representation of the dynamic resistance profile compared to the individual features used in other studies.

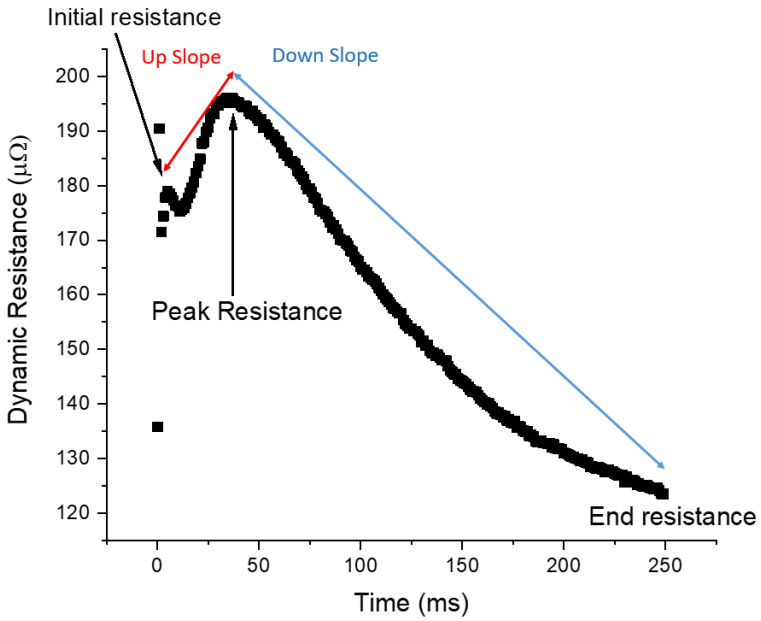

Figure 6.1 Different resistive features which can be measured using dynamic resistance measurement

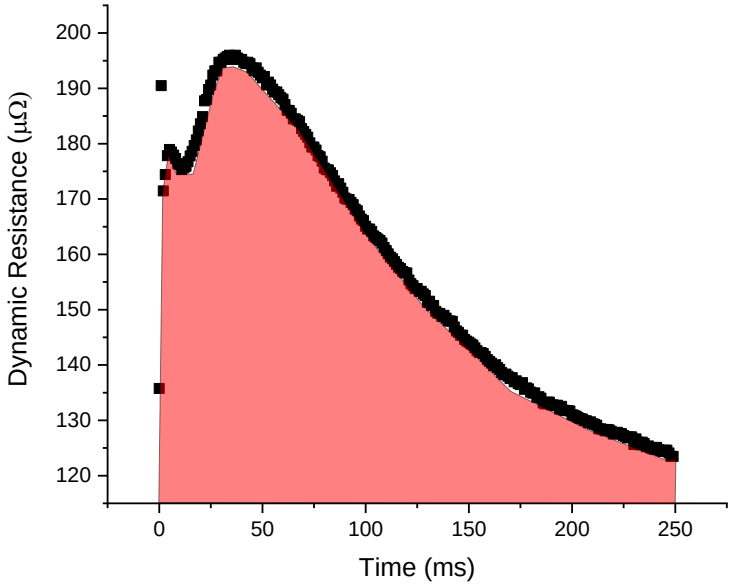

Figure 6.2 An illustration of heat input as the area under the dynamic resistance curve

6.3 Correlation Between Nugget size, Heat Input, and Welding Current

To confirm that the heat input analysis represents the welding cycle, the relationship between the heat input, nugget size, and welding current was examined (Fig. 6.3). At a lower welding current range (4-8 kA), a parabolic correlation was observed between the heat input and the welding current. This trend was expected because of the current term in the heat generation formula being squared (Eqn. 3.1). When the welding current was above 8 kA, the calculated heat input increased linearly with the welding current. At a higher welding current, increased electrode indentation and growth of nugget size caused this reduction in the dynamic resistance which slowed down the heat input growth, resulting in a linear correlation between the nugget size and welding current instead of the parabolic correlation observed at lower current range. The nugget size also has a linear relationship with the welding current below the expulsion condition (Fig. 6.3). With higher welding current, more heat is introduced into the weld region to promote melting of the base material, therefore increasing the nugget size. When entering the expulsion region, nugget growth was interrupted due to loss of

material and formation of a shunting path. When plotting the heat input and the nugget diameter curves in the same graph (Fig. 6.3), a clear overlap can be observed between the two curves where they both have a linear correlation with the welding current. This overlap allows the heat input to be used as an indicator for nugget size under the non-expulsion conditions.

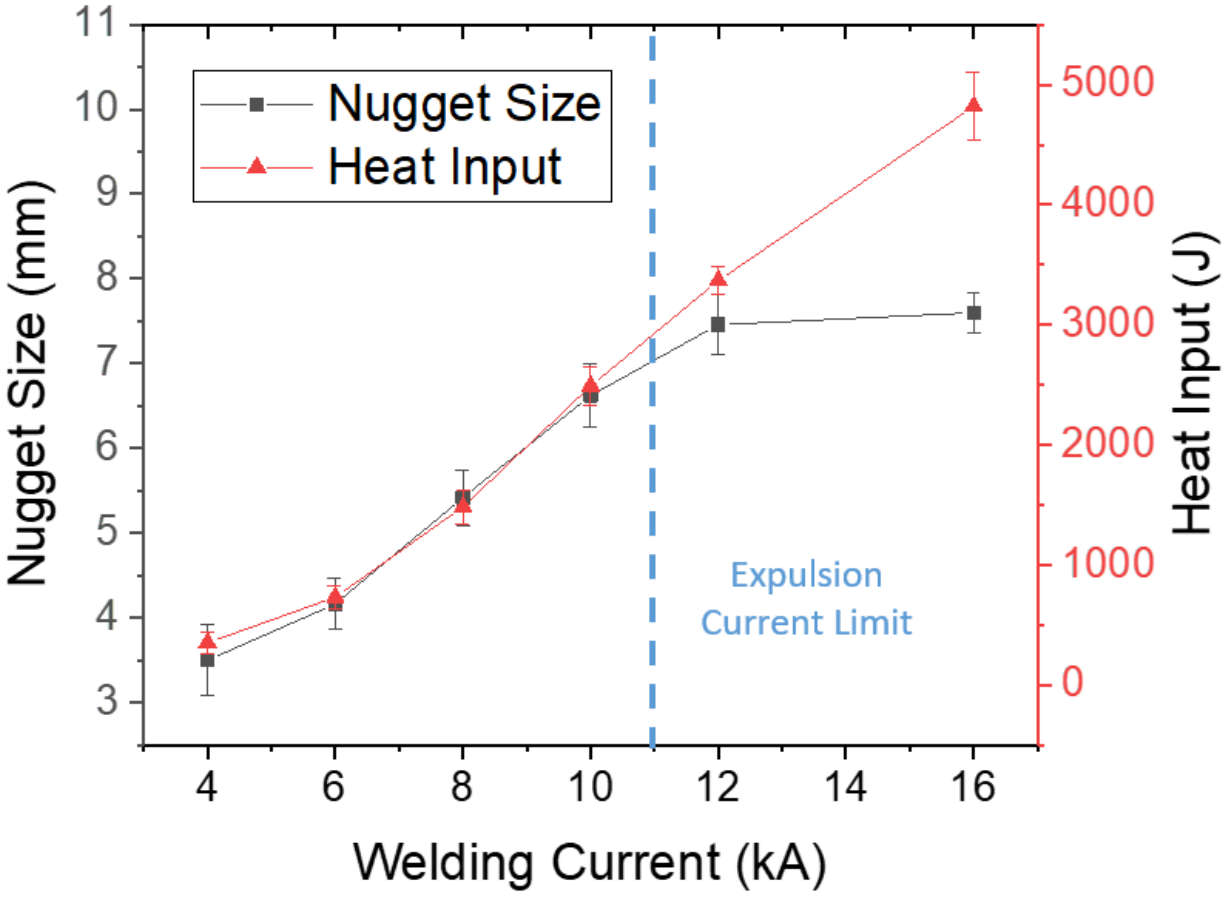

Figure 6.3 Correlation between nugget size (black), heat input (red), and welding current (the expulsion current limit is indicated by the blue dashed line).

6.4 Weld Monitoring and Correction Based on Heat Input Analysis

With the established relationship between the heat input and the nugget size, the heat input can be used to monitor and adjust the nugget size when an unexpected change in surface condition occurs. PHS samples with different heat-treatment times of 4, 7, and 10 min from chapter 5 were selected to

simulate the unexpected variations in the surface condition. Samples with the longest heat-treatment (10 min) time were selected as the baseline for this study. When welding with the same welding parameters, the heat input analysis reflected the change in heat-treatment conditions where a reduced heat input was observed for the shorter heat-treatment condition (4 & 7 min) due to their lower electrical resistance (Fig. 6.4a). The reduced heat input indicates that there is a potential to form of an undersized nugget if a shorter than designed heat-treatment time is used, which was confirmed through the nugget size measurement (Fig 6.4b).

To mitigate the variation in the nugget size due to the heat-treatment time change, a weld current correction was implemented, where the welding current was increased in the short and medium heat-treatment time conditions to increase their heat input and to normalize the heat input with respect to the measured baseline. After balancing the heat input (Fig 6.4a), the nugget sizes in the shorter heat-treatment time conditions have recovered to the baseline (Fig 6.4b). Therefore, the heat input analysis is capable of detecting surface condition variations and correcting undersized nuggets by balancing the heat input with respect to an established baseline.

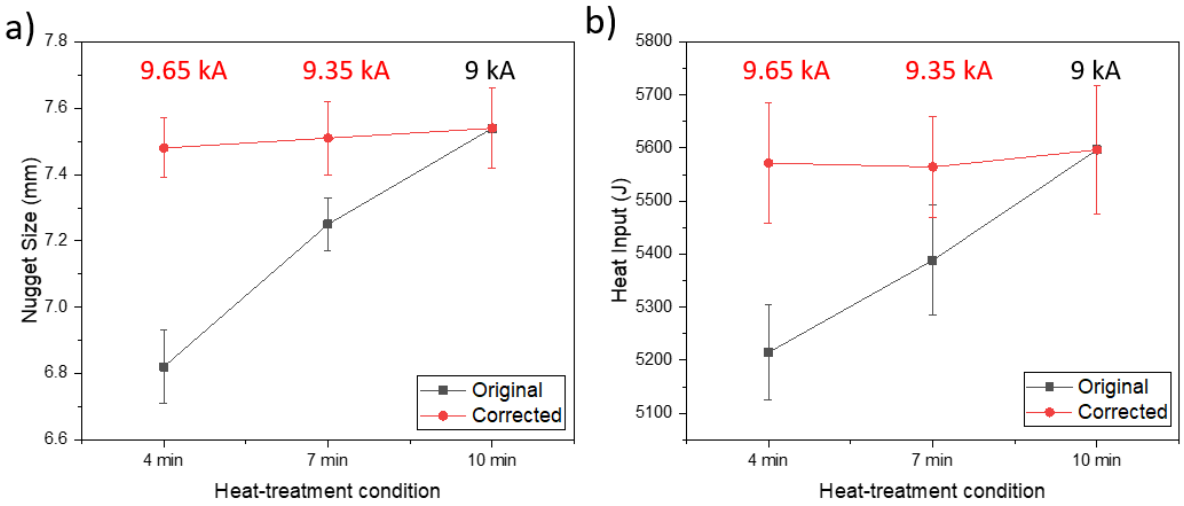

Figure 6.4 a) Heat input and b) nugget size of PHS spot welds using an identical welding parameter (black) and a corrected welding parameter (red)

6.5 Limitation of Heat Input Analysis

While the heat input analysis is capable of correcting nugget sizes based on the resistive feedback, understanding the limitations of this technique is important. The heat input analysis does not account for the difference in heat dissipation. As a proportion of the generated heat was lost through the electrode contact and the open environment, not all heat generated is used in forming the weld. Using solely the heat input implies the assumption of an equal heat dissipation in all conditions, which is not always the case. While not encountered in a laboratory setting, phenomena such as electrode mushrooming or unstable electrode force could potentially occur in a manufacturing environment. These phenomena affect the thermal contact condition between the electrode and the material surface, which influences the energy dissipation rate. Careful considerations are required to ensure the accuracy in the heat input analysis.

6.6 Summary

Heat input during welding can be computed based on the dynamic electric resistance measurement during the resistance spot welding process. This heat input measurement incorporates the different resistance features into a single value and is a good indicator of the weld performance given its correlation with the nugget size. The heat input analysis is capable of detecting surface condition changes due to the change in Zn diffusion layer. Balancing the heat input through a change in welding current corrected formations of undersized nuggets, resulting in the production of a consistent nugget size despite the potential variations in the surface condition.

Chapter 7 Conclusion and Recommendation

7.1 Effect of Internal Oxidation on Resistance Spot Welding

Internal oxidation on AHSS has been shown to reduce the heat generation in resistance spot welding, increasing the required current needed for welding. Internal oxidation promotes localized heating at the faying surface, which leads to surface melting. Surface melting reduces the contact resistance at the faying surface, which in turn reduces the overall heat generation during the welding process. This reduction in heat generation was only observed in the interface dominated region of the welding cycle, which occurs at the beginning of the weld cycle. As the weld cycle progressed into the nugget growth region, the difference in dynamic resistance was no longer observable. The overall reduction of heat input due to the presence of internal oxides was measured to be 80 J during the welding of the CMnSi steel in the annealed condition when compared to samples welded in the as-received condition. The reduction in heat generation leads to smaller nuggets being formed in samples in the annealed condition if the welding parameters are not adjusted. To prevent the formation of undersized nugget, the heat input must be increased by either increasing the welding current or extending the welding time. The corrected welding process window is shown in the form of a weld lobe.

7.2 Effect of Variation in Zn Diffusion Layer in Press-hardening Steel on its RSW Process

During the heat treatment process of PHS, Zn from the GA coating diffused into the steel matrix forming a diffusion layer comprised of a uniform α-Fe (Zn) solid-solution. The thickness and composition of the Zn diffusion layer were shown to be dependent on both the heat treatment time and the initial coating weight. A higher initial coating weight increased both the diffusion layer thickness and the Zn content in the diffusion layer, while increasing the heat-treatment time results in a thicker diffusion but reduced Zn content. When increasing the heat-treatment time, the lower Zn

concentration in the diffusion layer caused an increase in the surface contact resistance. Changes in the resistive behavior affected the welding process, which required less current to be needed to weld when the diffusion layer was thicker. When all heat treatment conditions were considered, the combined weld lobe had a width greater than 1.5 kA, exceeding the typical weld lobe of 1 kA used in the automotive industry for sufficient weld robustness. Even though heat treatment affected nugget size, due to differences in resistivity, if constant welding parameter were used tensile shear strength did not vary regardless of the heat-treating condition and nugget size. It has been found that samples with larger nugget experienced more severe martensite tempering in the heat-affected region, leading to a local reduction in material strength, compensating for the larger nugget size.

7.3 Use of Heat Input to Monitor and Correct Weld Parameters

The proposed heat input analysis based on the dynamic electrical resistance measured during RSW has been proven effective at monitoring the weld development given its linear correlation to the final nugget size within the non-expulsion region. The heat input analysis was shown to be effective at detecting undersized nuggets due to a variation in the Zn diffusion layer created by different heat-treatment conditions. From the heat input analysis, a corrected welding current is proposed which restored the nugget size to the established baseline.

7.4 Recommendations for future work

This work has shown that changing annealing time (from 240 s to 420 s) during selective oxidation has a minimal effect on the welding process. It is obvious that a critical annealing time exists where the surface melting mechanism transitions from the case observed in the as-received to one observed in the annealed condition. It is worthwhile to explore the minimum annealing time to trigger the surface melting mechanism.

This work has evaluated the behavior of internal oxidation without galvanizing of the substrate. Application of a Zn coating on the internally oxidized samples can introduce addition effects on the welding process. Presence of internal oxide can promote the diffusion of Zn from the coating into the grain boundary of the substrate, which may form potential liquid metal embrittlement that is detrimental to the weld quality. Future work can be performed on evaluating the effect of zinc-based coatings on the internally oxidized sample.

In monitoring and controlling of RSW using the current heat input analysis, the difference in heat dissipation was neglected. Investigations are necessary to confirm the effect of the potential factors that might influence the heat dissipation, such as electrode pressure and size, on the accuracy of the heat input analysis.

Bibliography

[1] "Office of Transportation and Air Quality. EPA and NHTSA Finalize Hisotric National Program to Reduce Greenhouse Gases and Improve Fuel Economy for Cars and Trucks," 2010.

[2] H. C. Kim and T. J. Wallington, "Life-cycle energy and greenhouse gas emission benefits of lightweighting in automobiles: Review and harmonization," *Environ. Sci. Technol.*, vol. 47, no. 12, pp. 6089–6097, 2013.

[3] D. A. Baker and T. G. Rials, "Recent advances in low-cost carbon fiber manufacture from lignin," *J. Appl. Polym. Sci.*, vol. 130, no. 2, pp. 713–728, 2013.

[4] I. N. Fridlyander, V. G. Sister, O. E. Grushko, V. V Berstenev, L. M. Sheveleva, and L. A. Ivanova, "Aluminum alloys: promising materials in the automotive industry," *Met. Sci. heat Treat.*, vol. 44, no. 9–10, pp. 365–370, 2002.

[5] D. Bhattacharya, "Microalloyed Steels for the Automotive Industry," *Tecnol. em Metal. Mater. e Mineração*, vol. 11, no. 4, pp. 371–383, 2015.

[6] J. L. Snoek, "On the decarburization of steel and related questions," *Physica*, vol. 8, no. 7, pp. 734–744, 1941.

[7] E. C. Nelson and N. R. Griffing, "Decarburization process for highchromium steel." Google Patents, 1962.

[8] N. Birks, G. H. Meier, and F. S. Pettit, *Introduction to the high temperature oxidation of metals*. Cambridge University Press, 2006.

[9] C. W. Lee, D. W. Fan, I. R. Sohn, S.-J. Lee, and B. C. De Cooman, "Liquid-metal-induced embrittlement of Zn-coated hot stamping steel," *Metall. Mater. Trans. A*, vol. 43, no. 13, pp. 5122–5127, 2012.

[10] J. Kondratiuk, P. Kuhn, E. Labrenz, and C. Bischoff, "Zinc coatings for hot sheet metal forming: Comparison of phase evolution and microstructure during heat treatment," *Surf. Coatings Technol.*, vol. 205, no. 17–18, pp. 4141–4153, 2011.

[11] O. Ighodaro, "Effects of Metallic Coatings on Resistance Spot Weldability of Hot Stamping Steel," *Thesis*, pp. 1–110, 2017.

[12] O. L. R. Ighodaro, E. Biro, and Y. N. Zhou, "Study and Applications of Dynamic Resistance Profiles During Resistance Spot Welding of Coated Hot-Stamping Steels," *Metall. Mater. Trans. A Phys. Metall. Mater. Sci.*, vol. 48, no. 2, pp. 745–758, 2017.

[13] J. Galán, L. Samek, P. Verleysen, K. Verbeken, and Y. Houbaert, "Advanced high strength steels for automotive industry," *Rev. Metal.*, vol. 48, no. 2, pp. 118–131, 2012.

[14] "Properties of advanced high strength steel."

[15] K. Sugimoto, M. Kobayashi, and S. Hashimoto, "Ductility and Strain-Induced Transformation in a High-Strength Transformation-Induced Plasticity-aided Dual-phase Steel," *Metall. Mater. Trans. A*, vol. 23, no. November, pp. 3085–3091, 1992.

[16] J. F. Lancaster, *Handbook of structural welding: processes, materials and methods used in the welding of major structures, pipelines and process plant*. Elsevier, 1997.

[17] E. C. Bain, "Functions of the alloying elements in steel (American Society for Metals,

Cleveland, OH),” 1939.

[18] K. E. THELNING, “Steels And Its Heat Treatment, 2aed,” *Butherworths, Mackays Gt. Britain Chatham Ltd*, 1984.

[19] D. W. Fan, H. S. Kim, and B. C. De Cooman, “A review of the physical metallurgy related to the hot press forming of advanced high strength steel,” *Steel Res. Int.*, vol. 80, no. 3, pp. 241–248, 2009.

[20] A. Turetta, S. Bruschi, and A. Ghiotti, “Investigation of 22MnB5 formability in hot stamping operations,” *J. Mater. Process. Technol.*, vol. 177, no. 1–3, pp. 396–400, 2006.

[21] J. S. Hou, “Resistance Spot Welding and In-Process Heat Treatment of Hot Stamped Boron Steel,” 2016.

[22] E. J. R. Robles, “Effect of Boron on the Microstructure and Properties of Ti-6Al-4V,” vol. 54, pp. 3150–3154, 2010.

[23] C. W. Lee, W. S. Choi, Y. R. Cho, and B. C. De Cooman, “Microstructure evolution of a 55wt.% Al-Zn coating on press hardening steel during rapid heating,” *Surf. Coatings Technol.*, vol. 281, pp. 35–43, 2015.

[24] W. Schatt, *Einführung in die Werkstoffwissenschaften*, 7th editio. 1991.

[25] W. C. Leslie, “The physical metallurgy of steels,” *Hemisph. Publ. Corp., 1981*, p. 396, 1981.

[26] G. Krauss, “Martensite in steel: strength and structure,” *Mater. Sci. Eng. A*, vol. 273–275, pp. 40–57, Dec. 1999.

[27] H. Bhadeshia and R. Honeycombe, *Steels: microstructure and properties*. Butterworth-Heinemann, 2017.

[28] G. Krauss, “Martensite in steel: strength and structure,” *Mater. Sci. Eng. A*, vol. 273–275, pp. 40–57, Dec. 1999.

[29] “Fe-C binary phase diagram.” [Online]. Available: http://www.calphad.com/iron-carbon.html.

[30] Y. Prawoto, N. Sato, I. Otani, and M. Ikeda, “Carbon Restoration for Decarburized Layer in Spring Steel,” *J. Mater. Eng. Perform.*, vol. 13, no. October, pp. 627–636, 2004.

[31] A. P. Yadav, A. Nishikata, and T. Tsuru, “Degradation mechanism of galvanized steel in wet-dry cyclic environment containing chloride ions,” *Corros. Sci.*, vol. 46, no. 2, pp. 361–376, 2004.

[32] N.-Y. Tang, “Characteristics of continuous-galvanizing baths,” *Metall. Mater. Trans. B*, vol. 30, no. 1, pp. 144–148, 1999.

[33] M. A. Bright, G. C. Becherer, and R. L. Grodeck, “Galvanizing bath apparatus.” Google Patents, 2013.

[34] S. M. A. Shibli, B. N. Meena, and R. Remya, “A review on recent approaches in the field of hot dip zinc galvanizing process,” *Surf. Coatings Technol.*, vol. 262, pp. 210–215, 2015.

[35] “Continuous galvanizing line setup.” [Online]. Available: http://image.ec21.com/company/g/gt/gte/gteco/upimg/1_01b.jpg.

[36] C. E. Jordan and A. R. Marder, “Morphology development in hot-dip galvanneal coatings,” *Metall. Trans. A (Physical Metall. Mater. Sci. States)*, vol. 25, no. 5, 1994.

[37] Y. Y. Chang, W. J. Cheng, and C. J. Wang, “Growth and surface morphology of hot-dip Al-Si on 9Cr-1Mo steel,” *Mater. Charact.*, vol. 60, no. 2, pp. 144–149, 2009.

[38] C. J. Wang and S. M. Chen, “The high-temperature oxidation behavior of hot-dipping Al-Si coating on low carbon steel,” *Surf. Coatings Technol.*, vol. 200, no. 22-23 SPEC. ISS., pp. 6601–6605, 2006.

[39] I. S. Hwang, M. J. Kang, and D. C. Kim, “Expulsion reduction in resistance spot welding by controlling of welding current waveform,” *Procedia Eng.*, vol. 10, pp. 2775–2781, 2011.

[40] A. H. Wang and T. M. Yue, “YAG laser cladding of an Al-Si alloy onto an Mg/SiC composite for the improvement of corrosion resistance,” *Compos. Sci. Technol.*, vol. 61, no. 11, pp. 1549–1554, 2001.

[41] D. W. Fan and B. C. De Cooman, “State-of-the-knowledge on coating systems for hot stamped parts,” *Steel Res. Int.*, vol. 83, no. 5, pp. 412–433, 2012.

[42] J. Maki, J. Mahieu, B. C. De Cooman, and S. Claessens, “Galvanisability of silicon free CMnAl TRIP steels,” *Mater. Sci. Technol.*, vol. 19, no. 1, pp. 125–131, 2003.

[43] M. Dubois and L. Bordignon, “Process Window for Pre-Oxidation for a Full Radiant Tube Furnace,” pp. 2201–2212, 2018.

[44] B. C. De Cooman, “The surface and sub-surface structure of continuously annealed sheet steel: implications for galvanizing and galvannealing.,” *Trans. Indian Inst. Met.*, vol. 59, no. 5, pp. 769–786, 2006.

[45] G. Seyed Mousavi and J. R. McDermid, “Selective Oxidation of a C-2Mn-1.3Si (Wt Pct) Advanced High-Strength Steel During Continuous Galvanizing Heat Treatments,” *Metall. Mater. Trans. A Phys. Metall. Mater. Sci.*, vol. 49, no. 11, pp. 5546–5560, 2018.

[46] E. Thomson, “Apparatus for electric welding.” Google Patents, 1916.

[47] M. Pouranvari and S. P. H. Marashi, “Critical review of automotive steels spot welding: process, structure and properties,” *Sci. Technol. Weld. Join.*, vol. 18, no. 5, pp. 361–403, 2013.

[48] N. T. Williams and J. D. Parker, “Review of resistance spot welding of steel sheets Part 1 Modelling and control of weld nugget formation,” *Int. Mater. Rev.*, vol. 49, no. 2, pp. 45–75, 2004.

[49] “A typical resistance spot welding setup.” [Online]. Available: http://mechanicalinventions.blogspot.com/2014/09/resistance-spot-welding-rsw-working-principle.html.

[50] Z. Han, J. Orozco, J. E. Indacochea, and C. H. Chen, “Resistance Spot Welding: A Heat Transfer Study,” *Weld. J.*, vol. 73, pp. 362s-371s, 1989.

[51] W. F. Savage, E. F. Nippes, and F. A. Wassell, “Dynamic Contact Resistance of Series Spot Welds,” *Weld. Res. Suppl.*, pp. 365–370, 1977.

[52] E. Crinon and E. J. T., “The effect of surface roughness, oxide film thickness and interfacial sliding on the electrical contact resistance of aluminium,” *Mater. Sci. Eng. A*, vol. 242, no. 1–2, pp. 121–128, 1998.

[53] J. K. W. Choi, N. Y. Zhou, and A. P. Gerlich, “INTERPRETING DYNAMIC RESISTANCE TO MONITOR SHUNTING AND EDGE PROXIMITY,” in *Sheet Metal Welding*

Conference, 2018, pp. 1–11.

[54] A. G. Livshits, “Universal Quality Assurance Method for Resistance Spot Welding Based on Dynamic Resistance,” *Weld. Res. Suppl.*, pp. 383–390, 1997.

[55] S. S. Babu, M. L. Santella, Z. Feng, B. W. Riemer, and J. W. Cohron, “Empirical model of effects of pressure and temperature on electrical contact resistance of metals,” *Sci. Technol. Weld. Join.*, vol. 6, no. 3, pp. 126–132, 2004.

[56] H. Nied, “The finite element modeling of the resistance spot welding process,” *Annu. AWS Conv.*, pp. 123–133, 1984.

[57] American Welding Society, “AWS D8.9 Test Method for Evaluating the Resistance Spot Welding Behavior of Automotive Sheet Steel Materials.” .

[58] N. T. Williams and J. D. Parker, “Review of resistance spot welding of steel sheets Part 1 Modelling and control of weld nugget formation,” *Int. Mater. Rev.*, vol. 49, no. 2, pp. 45–75, 2004.

[59] M. Pouranvari, S. M. Mousavizadeh, S. P. H. Marashi, M. Goodarzi, and M. Ghorbani, “Influence of fusion zone size and failure mode on mechanical performance of dissimilar resistance spot welds of AISI 1008 low carbon steel and DP600 advanced high strength steel,” *Mater. Des.*, vol. 32, no. 3, pp. 1390–1398, 2011.

[60] H. Zhang, X. Qiu, F. Xing, J. Bai, and J. Chen, “Failure analysis of dissimilar thickness resistance spot welded joints in dual-phase steels during tensile shear test,” *Mater. Des.*, vol. 55, pp. 366–372, 2014.

[61] N. T. Nguyen, D. Y. Kim, J. H. Song, K. H. Kim, I. H. Lee, and H. Y. Kim, “NUMERICAL PREDICTION OF VARIOUS FAILURE MODES IN SPOTWELDED METALS,” *Int. J. Automot. Technol.*, vol. 13, no. 3, pp. 459–467, 2012.

[62] K. Han, I. Ohnuma, K. Okuda, and R. Kainuma, “Experimental determination of phase diagram in the Zn-Fe binary system,” *J. Alloys Compd.*, vol. 737, pp. 490–504, 2018.

[63] S. Aslanlar, “The effect of nucleus size on mechanical properties in electrical resistance spot welding of sheets used in automotive industry,” *Mater. Des.*, vol. 27, no. 2, pp. 125–131, 2006.

[64] M. I. Khan, M. L. Kuntz, and Y. Zhou, “Effects of weld microstructure on static and impact performance of resistance spot welded joints in advanced high strength steels,” *Sci. Technol. Weld. Join.*, vol. 13, no. 3, pp. 294–304, 2008.

[65] V. H. Hernandez, S. K. Panda, Y. Okita, and N. Y. Zhou, “A study on heat affected zone softening in resistance spot welded dual phase steel by nanoindentation,” *J. Mater. Sci.*, vol. 45, pp. 1638–1647, 2010.

[66] H. Zhang and J. Senkara, *Resistance welding: fundamentals and applications*. CRC press, 2011.

[67] R. J. Ditchburn, S. K. Burke, and C. M. Scala, “NDT of welds: State of the art,” *NDT E Int.*, vol. 29, no. 2, pp. 111–117, 1996.

[68] R. Ludwig and W. Lord, “A finite-element formulation for the study of ultrasonic NDT systems,” *IEEE Trans. Ultrason. Ferroelectr. Freq. Control*, vol. 35, no. 6, pp. 809–820, 1988.

[69] L. B. Cherry, “Method and apparatus for determining the quality of a weld or solder joint by measurement of the dynamic resistance of the joint.” Google Patents, 1965.

[70] S. Bhattacharya and D. R. Andrews, “Resistance-Weld Quality Monitoring,” *Sheet Met. Ind.*, pp. 400–466, 1972.

[71] D. R. Andrews and S. Bhattacharya, “Quality Control-Resistance-Weld Monitoring for Production,” *Met. Constr. Br. Weld. J.*, pp. 172–175, 1973.

[72] D. W. Dickinson, J. E. Franklin, and A. Stanya, “Characterization of Spot Welding Behavior by Dynamic Electrical Parameter Monitoring,” *Weld. Res. Suppl.*, pp. 170–176, 1980.

[73] S. A. Gedeon and T. W. Eagar, “Resistance spot welding of galvanized steel: Part I. Material variations and process modifications,” *Metall. Trans. B*, vol. 17, no. 4, pp. 879–885, 1986.

[74] J. R. McDermid, C. Thomsen, X. Han, and N. Y. Zhou, “Internal Oxidation Effects on Forming and Welding Behaviour of Advanced High Strength Steel,” in *GAP meeting*, 2018.

[75] C. A. C. Sequeira, A. M. G. Pacheco, and C. M. . G. S. Nunes, “Formation of Diffusion Coatings on Iron and Steel: 2 Theoretical Considerations,” *Surf. Eng.*, vol. 3, no. 3, pp. 247–260, 1987.

[76] M. H. Razmpoosh, A. Macwan, E. Biro, and Y. Zhou, “Effect of coating weight on fiber laser welding of Galvanneal-coated 22MnB5 press hardening steel,” *Surf. Coatings Technol.*, vol. 337, no. October 2017, pp. 536–543, 2018.

[77] P. Shewmon, *Diffusion in solids*. Springer, 2016.

[78] M. Zhou, S. Hu, and H. Zhang, “Critical specimen sizes for tensile-shear testing of steel sheets,” *Weld. J.*, vol. 78, no. 9, pp. 305S-313S, 1999.